Stress-induced ribosome degradation in *Bacillus subtilis* is mediated by the RNase Y-specificity complex.

Fabián A. Cornejo[1,#,*], Kristina Driller[1,2,#], Rina Ahmed-Begrich[1], Katja Schmidt[1], Michael Jahn[1], Vivekanandan Shanmuganathan[1], Karin Hahnke[1], Florian Kondrot[1], Thomas F. Wulff[1], Sebastian Rämisch[1], Kathirvel Alagesan[1], Emmanuelle Charpentier[1,3], and Kürşad Turgay[1,2,*]

[1]Max Planck Unit for the Science of Pathogens, Berlin, Germany

[2]Leibniz Universität Hannover, Institute of Microbiology, Hannover, Germany

[3]Humboldt-Universität zu Berlin, Institute of Biology, Berlin, Germany

[#]These authors equally contributed to this work

**Correspondence to*: cornejo@mpusp.mpg.de, turgay@mpusp.mpg.de

Abstract

Limiting the synthesis and activity of ribosomes is crucial for adaptation to stresses, such as heat or nutrient starvation. In *Bacillus subtilis,* this can be achieved through the coordinated action of the alarmones (p)ppGpp and the transcription factor Spx. Here, we performed a genetic screen to uncover novel factors contributing to the heat shock response of *B. subtilis*. We identified the Y-complex, which confers specificity to the endonuclease RNase Y, as a critical player during stress conditions, such as heat or transition into stationary phase. This protein complex is required for processing diverse RNAs, notably the maturation of mRNAs encoding proteins involved in translation and metabolism. We further demonstrate that the Y-complex and RNase Y initiate the degradation of rRNAs of mature ribosomes, lowering their abundance. We propose that the Y-complex is a regulatory hub that modulates gene expression, adjusts protein synthesis and resource allocation.

Keywords: *Bacillus subtilis*, Ribosome, Stress response, Y-complex, RNase Y, Ribosome degradation, Heat shock, (p)ppGpp

Introduction

Bacteria can sense, adapt to, and survive stressful environmental changes facilitated by various general and specific stress response systems. Proteotoxic stresses, like high temperatures, significantly disrupt protein folding and can lead to the formation of toxic protein aggregates. Chaperones and proteases are expressed as a response due to the inactivation of the transcriptional repressors HrcA and CtsR in *Bacillus subtilis*[1–4]. The activation of the protein quality control (PQC) allows the refolding of un- or misfolded proteins by different chaperone systems or the degradation of irreparable proteins through AAA+ protease complexes like ClpCP[5,6].

In addition to the repairing or removal of protein aggregates, inhibiting translation is crucial for survival during proteotoxic stresses, as it can alleviate the extra load on the PQC system[7–10]. In *Bacillus subtilis*, the nucleotide second messengers guanosine tetraphosphate and guanosine pentaphosphate, collectively referred to as (p)ppGpp, and the transcription factor Spx independently regulate synthesis and activity of ribosomes during stress[7,11]. Spx is a redox-sensitive heat shock transcription factor that controls the expression of redox chaperones and simultaneously represses transcription of translation-related genes during oxidative and heat shock response[11–14].

The alarmones (p)ppGpp were initially discovered to be synthesized during amino acid starvation, but more recently, it was observed that their synthesis is also induced by protein folding stresses, such as heat or oxidative stress[7]. During heat stress, their accumulation results in increased thermoresistance, inhibition of translation, and a reduction in protein aggregation[7]. (p)ppGpp inhibit translation by binding to specific GTPases (e.g. IF2, RbgA)[15–17]. Furthermore, (p)ppGpp accumulation can lead to decreased transcription of e.g. rRNA and ribosomal protein (r-protein) transcripts by inhibiting GTP biosynthesis and reducing its levels[18,19]. This downregulation of translation is an important component of the response to nutrient scarcity as well as heat shock.

In this study, we aimed to identify new genes or pathways involved in the heat shock response using a genetic screen that reports on fitness. We identified that the Y-complex (RicAFT-complex), which interacts with the endonuclease RNase Y and conveys substrate specificity, plays a role in the heat shock response. We demonstrate further that the Y-complex regulates ribosome levels by initiating ribosome degradation during nutrient depletion or heat shock. Mutants lacking a Y-complex member show increased ribosome levels before and during heat shock, increasing the burden on the PQC system and, in consequence, protein aggregation during heat stress. These findings not only indicate the importance of RNases during stress response but also emphasize that controlling the stability of RNA is an important general mechanism to modify cellular function.

Results

The Y-complex is necessary for survival during heat shock

To identify genes that play a role in the heat shock response, we used the BKE single-mutant library[20], which includes a barcoded deletion cassette for each non-essential gene in *B. subtilis*. All gene deletion mutant strains were pooled, grown at 30°C, and subjected to a mild heat shock at 50°C during the mid-exponential phase, while a control was maintained at 30°C. Relative fitness scores for each gene deletion in the pooled population were calculated by quantifying each barcode at different temperatures (**Fig. 1A, Supplementary Table 1**). The relative fitness of the heat shocked cultures compared to the cultures grown at 30°C was used to identify genes whose deletion results in a change in fitness during heat shock (**Fig. 1A-B, Supplementary Table 1**).

We observed that *B. subtilis* strains lacking the genes coding for the heat shock transcriptional repressors HrcA or CtsR exhibit higher fitness at 50°C compared to 30°C (**Supplementary Fig. 1A**), consistent with their known regulatory role. In contrast, deletion of the genes coding for the DnaK chaperone system, the protease ClpP, and the adaptor protein complex McsA-McsB show greater sensitivity to increased temperatures (**Supplementary Fig. 1B**), demonstrating that our screening approach can identify genes with already known heat-shock phenotypes[21–23].

The control of transcription initiation by transcription factors has been well established[24]. However, the contribution of RNA stability in stress response is not well understood. Interestingly, six mutants lacking RNases or RNase-regulating genes exhibit differential fitness at 50°C compared to 30°C (**Fig. 1B)**. The deletion of RNase Mini-III (Δ*mrnC)* results in lower fitness at 30°C, whereas its fitness remains unaffected at 50°C. Deletions of RNase J2 (Δ*rnjB)*, the nano-RNase A (Δ*nrnA*), and the RNA pyrophosphohydrolase and (p)ppGpp hydrolase NahA (Δ*yvcI*) exhibit reduced fitness during increased temperatures (**Fig. 1B**).

One of the mutants with the lowest fitness score at 50°C is Δ*ymcA* (**Fig. 1B**). YmcA (RicA) interacts with YaaT (RicT) and YlbF (RicF) to form the Y-complex, which associates with the endonuclease RNase Y for maturation of polycistronic mRNA and riboswitches[25,26]. In addition, we also identified Δ*yaaT* in our screen (**Fig. 1B**). We could confirm the heat sensitivity of all three deletion mutants of the Y-complex genes in single-culture experiments during a severe heat shock at 54°C (**Fig. 1C**).

Identification of Y-complex-dependent cleavages at late exponential and transition phases

96 We evaluated the growth of all three strains lacking the Y-complex encoding genes. They
97 exhibit a similar growth defect that begins at the end of the exponential phase and continues
98 during transition phase until the stationary phase (**Fig. 2A**)**.** Given that this complex associates
99 with the endonuclease RNase Y and regulates substrate selection[26], we investigated Y-
100 complex-dependent cleavages in the late exponential and transition phase (**Fig. 2A**) using the
101 ISCP (Identification of Specific Cleavage Positions) approach[27]. We compared the coverage
102 of RNA 3' and 5' ends in the WT and Δ*ymcA* mutant, and the ends significantly reduced in the
103 Δ*ymcA* were classified as putative Y-complex-dependent cleavages (**Supplementary Table**
104 **2**). It is worth noting that deleting any member of the Y-complex results in a significant decrease
105 in the processing of substrate RNA[26]. When a transcript is cleaved, it results in two products:
106 one is quickly degraded by exonucleases, while the other is stabilized[27]. Consequently, it is
107 not always possible to detect both 5' and 3' ends after cleavage.

108 We identified 221 and 258 Y-complex-dependent ends in late exponential and transition
109 phases, with six also detected in a previous study at the mid-exponential phase[26]
110 (**Supplementary Table 3**). In the late exponential phase, 5' and 3' ends are almost equally
111 distributed, yet more 5*'* ends are detected in the transition phase (**Fig. 2B**).

112 It is known that the Y-complex and RNase Y generate fragments with differential stability in the
113 mid-exponential phase[26]. Here, we evaluated the stability of the resulting fragments in the late
114 exponential and transition phases by calculating the ratio of coverage upstream and
115 downstream of the cleavage site (**Supplementary Table 2**). We observed a trend toward
116 stabilizing downstream fragments. However, upstream fragments can also be stabilized, but
117 to a lesser extent (**Supplementary Fig. 2A**). The ISCP method differentiates processing sites
118 with blunt ends (Unique, U-type) or when it was further processed by exonucleases[27] (Stepped,
119 S-type). Most S-types were found at the 3' ends, suggesting further processing by
120 exonucleases, while most U-types were detected at 5' ends (**Fig. 2C**). This is consistent with
121 the trend to stabilise the downstream fragment (**Supplementary Fig. 2A**).

122 The Y-complex could target a particular sequence motif, thereby helping to recognize specific
123 substrates. However, a motif search using U-type ends resembles the simple motif described
124 for RNase Y in *B. subtilis*[28], *S. aureus*[29]*,* and *S. pyogenes*[27], being most likely a G upstream of
125 the cleavage site (**Supplementary Fig. 2B**). Given the simple sequence motif, we investigated
126 whether cleavages occur randomly in longer or more abundant transcripts. Notably,
127 approximately 81% of targeted transcripts are cleaved only once, about 16% twice, and very
128 few are cleaved multiple times (**Supplementary Fig. 2C)**. Neither the length nor the
129 abundance of a transcript predicts whether it is cleaved, suggesting that other factors influence
130 where cleavages occur (**Supplementary Fig. 2D-E, Supplementary Table 4**). Recent studies

131 have shown that the cleavage efficiency is multifactorial, depending on the sequence and
132 secondary structures surrounding the cleavage site[28,30].

133 As we observed that RNA processing could result in fragments with different stability
134 (**Supplementary Fig. 2A**), we wondered if this could be a consequence of secondary
135 structures protecting them from exonucleases. We used U-type ends and compared transcripts
136 with the same cleavage motif but not cleaved as controls. For the 5' ends, a strong decrease
137 in the minimum free energy ~25 nt downstream of the cleavage site indicated a possible
138 secondary structure, while the upstream fragment remained similar to the control (**Fig. 2D**).
139 The upstream fragment's lower stability may be due to its lack of secondary structure, making
140 it accessible to 3'-5' exonucleases. For the 3' ends, the more stable upstream fragment could
141 form a possible secondary structure starting 10 nt upstream of the cleavage site (**Fig. 2D**). The
142 generation of mRNA fragments with different stability might have a regulatory role in gene
143 expression.

144 **Y-complex-mediated transcript cleavages and mRNA maturation**

145 Most detected Y-complex-dependent ends are inside ORFs, mainly in polycistronic mRNAs
146 (**Fig. 2E-F**), confirming the role of the Y-complex in the maturation and stoichiometry regulation
147 of co-transcribed genes[26]. An example is the *cggR-gapA* transcript, where the Y-complex
148 mediates cleavage in the coding sequence of *cggR* near the stop codon[25,26]. Cleavage renders
149 the *cggR* fragment less stable compared to the *gapA* fragment (**Supplementary Fig. 3A**),
150 thereby uncoupling the transcript levels of these co-transcribed genes. Interestingly, we
151 observed other cleavages generating similar uncoupling of transcripts, such as in the gene
152 encoding the endonuclease YloC (**Supplementary Fig. 3B**, **Supplementary Table 2)**. In
153 addition, cleavages in genes transcribed as monocistronic mRNAs, such as *guaB,* suggest
154 that the Y-complex could initiate their degradation (**Supplementary Fig. 3C**, **Supplementary**
155 **Table 2**).

156 We observe Y complex-dependent processing in 5', 3', and internal UTRs (**Fig. 2F**). Cleavages
157 in 5' UTR suggest a possible regulatory role by decreasing the abundance of the mRNA
158 containing them, as already described for riboswitches[26,31], or by producing a shorter version
159 of a 5' UTR, which could affect gene expression. Processing of 3' and internal UTR could
160 influence mRNA stability and polycistronic mRNA maturation. We observed that some 3' UTR
161 cleavages are located upstream of the Rho-independent terminator, decreasing the stability of
162 the upstream fragment and leaving an apparent more stable downstream fragment that
163 includes its terminator structure, as observed for *trxB* (**Supplementary Fig. 3D**). This
164 phenomenon has been observed in *E. coli*, where RNase E cleaves upstream of the Rho-
165 independent terminator[32,33].

166 In polycistronic mRNA maturation, we observed that Y-complex processes internal UTRs,
167 decoupling the RNA levels of coding fragments (**Supplementary Fig. 3E-F**). For example, the
168 *bipA-ylaH* transcript is cleaved 21 nt after the *bipA* stop codon, rendering the upstream
169 fragment less stable than the *ylaH* fragment (**Supplementary Fig. 3E**). We also observed a
170 cleavage between the *fusA* (EF-G) and *tufA* (EF-Tu) genes, both coding for translation
171 elongation factors (**Supplementary Fig. 3F**).

172 **The Y-complex targets translation and metabolism-related genes in the late exponential**
173 **phase**

174 We wondered if the Y-complex primarily processes transcripts bearing genes with specific
175 functions required for switching the growth phase. Therefore, we conducted an
176 overrepresentation analysis and observed that the most significantly enriched categories
177 pertain to "Metabolism" and "Information processing" (**Fig. 2G, Supplementary Fig. 4A,**
178 **Supplementary Table 5**). Overall, the Y-complex is predominantly involved in the processing
179 of operons encoding genes for carbon metabolism (e.g., glycolysis and gluconeogenesis),
180 nucleotide metabolism (e.g., pyrimidine and purine biosynthesis), and amino acid biosynthesis
181 and utilization (**Fig. 2G**). This allows adjusting the utilization and biosynthesis of nutrients when
182 they become limited. In addition, all transcripts containing rRNA and ~50% of transcripts
183 carrying genes encoding translation factors and r-proteins are processed by the Y-complex
184 (**Fig. 2G**).

185 The reduced RNA processing in the *ymcA* deletion strain results in significant changes in the
186 transcriptome (**Supplementary Fig. 4B, Supplementary Table 6-7**). Consequently,
187 transcripts of certain pathways related to metabolism and translation, among others, show
188 maturation events that depend on the Y-complex and also demonstrate differential expression
189 upon deletion of *ymcA* (**Fig. 2G**, **Supplementary Fig. 4B**). This may result from either a direct
190 or indirect effect of decreased RNA maturation events. Our results suggest that the Y-complex
191 and RNase Y are important for transitioning to the stationary phase by processing transcripts
192 related to translation and metabolism, which may impact their stability and/or gene expression.

193 **The Y-complex targets ribosomes for degradation**

194 Several Y complex-dependent cleavages were detected in the rRNA sequence during both
195 growth phases, most of them being in the 23S rRNA during the late exponential phase (**Fig.**
196 **3A**). We detected cleavages in specific helices in the 23S and 16S rRNA, mainly in loops of
197 hairpin structures (**Supplementary Fig. 5A-B**). These helices are accessible and primarily
198 located close to the A-site and the interface between the two ribosomal subunits
199 (**Supplementary Fig. 6**), which could be recognized and cut by the Y-complex with the
200 endonuclease RNase Y. These cleavages will most likely destabilize the ribosome structure.

201 Generating free 5' and 3' RNA ends, which are substrates for exonucleases such as PNPase,
202 RNase R, and RNase J, will result in further RNA degradation and ribosome disassembly,
203 releasing the ribosomal proteins as well.

204 We confirmed the observed rRNA degradation via northern blots of 23S or 16S rRNA (**Fig. 3B**,
205 **Supplementary Fig. 7A**). Deletion of *ymcA* strongly reduces the presence of rRNA
206 degradation intermediates during the late exponential phase. As ribosomes are assembled co-
207 transcriptionally[34], we inhibited transcription by adding rifampicin to cultures at the late
208 exponential phase. We observed that stopping transcription does not affect rRNA degradation
209 of the 23S and even raises the levels of 16S degradation intermediates, indicating that mature
210 ribosomes are degraded (**Fig. 3B**, **Supplementary Fig. 7A**). The Y-complex protein YaaT
211 interacts more stably with RNase Y in the membrane than YmcA and YlbF[35]. We tagged YaaT
212 with a C-terminal FLAG and identified interacting proteins during the late exponential phase by
213 pull-down (**Supplementary Fig. 7B, Supplementary Table 8**). We observed that YaaT
214 captures other Y-complex members (YmcA, YlbF), RNase Y, and components of the dynamic
215 degradosome complex, including enolase and PNPase. Interestingly, r-proteins are also
216 observed in the pull-down experiment, suggesting the Y-complex might target ribosomes to
217 RNase Y for initiation of rRNA degradation after exponential growth (**Supplementary Fig. 7B**).

218 Cleavages within mature rRNA can trigger ribosome disassembly and degradation, which,
219 during the transition phase, coincides with translation downregulation through reduced
220 synthesis and inhibition of ribosome activity. This suggests that the Y-complex may be involved
221 in reducing ribosome levels to accommodate the new, slower growth rate. Therefore, we
222 quantified ribosome content by measuring the abundance of all r-proteins via mass
223 spectrometry (**Supplementary Table 9**). When *B. subtilis* shifts from exponential to the
224 transition phase, we observed a coordinated reduction in r-protein levels (**Fig. 3C**), indicating
225 a decrease in ribosome levels. This reduction is highly impaired in Δ*ymcA* (**Fig. 3C**), where the
226 levels of r-proteins do not decline to the same degree as in the WT, likely due to the reduced
227 degradation of ribosomes.

228 Accumulation of (p)ppGpp leads to inhibition of transcription of rRNA and r-proteins[19,36] upon
229 shortages of nutrients during the transition to the stationary phase. To test if the deletion of
230 *ymcA* is interfering with this transcriptional downregulation, we measured the promoter activity
231 of the rRNA promoters *rrnJ* and *rrnB* and r-protein promoters of *rplK*, *rplJ*, and *rpsJ*. All these
232 promoters show similar downregulation in the late exponential and transition phases in both
233 WT and Δ*ymcA* strains (**Fig. 3D-E**, **Supplementary Fig. 7C-E**), confirming that their
234 transcriptional control remains unaffected and is not the cause of the increased ribosome
235 amounts in the Δ*ymcA* strain.

236 Notably, we observed that the increased levels of ribosomes in a Δ*ymcA* strain led to the
237 accumulation of hibernating 100S ribosomes during the transition phase (**Fig. 3F**). This 100S
238 is no longer observed after the deletion of the gene encoding the hibernation factor *hpf*, which
239 triggers their formation[37,38] (**Supplementary Fig. 7F**). The presence of hibernating ribosomes
240 at this time point indicates that functional and superabundant ribosomes in the Δ*ymcA* strain
241 are sequestered away from the actively translating pool through hibernation.

242 **(p)ppGpp and the Y-complex play a crucial role in regulating the levels of ribosomes**

243 Since ribosome levels and translation are lowered by (p)ppGpp under nutrient limitation or
244 other stresses, we wondered if there is a genetic interaction between the two systems. Deleting
245 *ymcA* in a strain that cannot synthesize (p)ppGpp [(p)ppGpp^0] leads to an even stronger growth
246 defect during the transition phase (**Fig. 4A**). The (p)ppGpp^0 strain, like Δ*ymcA*, shows impaired
247 reduction of ribosome levels during the transition phase (**Fig. 4B**). The double mutant
248 (p)ppGpp^0 Δ*ymcA* shows almost no reduction in ribosome quantities during this growth phase
249 (**Fig. 4B-C**). The same is observed when the r-protein mass fraction is calculated at the
250 transition phase (**Fig. 4D**). These experiments suggest that the Y-complex and (p)ppGpp
251 control ribosome levels and translation independently during post-exponential growth. The
252 absence of regulation by both systems results in a severe growth defect.

253 **Increased ribosome levels lead to protein aggregation during heat shock**

254 Since we discovered the Δ*ymcA* strain in a competition experiment during heat shock, we
255 explored whether the Y-complex is involved in lowering ribosome levels upon proteotoxic
256 stress. We evaluated the degradation of 23S and 16S rRNA by the Y-complex before and after
257 heat shock (**Fig. 5A**, **Supplementary Fig. 8A**). After 15 minutes at 50°C, degradation
258 intermediates are observed in the WT but not in Δ*ymcA*, confirming a role of the Y-complex in
259 degrading ribosomes during heat stress (**Fig. 5A**). Comparing r-protein mass fractions before
260 and during heat shock shows that both WT and Δ*ymcA* downregulate ribosome levels during
261 the experiment. Overall, there are increased levels of r-proteins in the Δ*ymcA* strain already
262 before the heat shock (**Fig. 5B**), which suggests a role of the Y-complex in maintaining
263 ribosome levels during normal growth. Notably, the levels and induction of known heat-shock-
264 regulated proteins are not affected in the *ymcA* deletion (**Fig. 5C, Supplementary Table 10,**
265 **Supplementary Fig. 8B**). This suggests that chaperone and protease induction during heat
266 stress in the Δ*ymcA* strain is intact.

267 The downregulation of translation is crucial to limit the increased burden of misfolding and
268 aggregation-prone nascent polypeptide chains on the PQC system. In agreement, a (p)ppGpp^0
269 strain shows increased aggregate formation during heat shock[7]. We quantified the relative
270 amount of aggregated proteins before and after 15 minutes of severe heat shock at 54°C and

271 observed that the Δ*ymcA* strain contained significantly higher amounts of aggregated proteins
272 already prior to heat exposure (**Fig. 5D**). This is consistent with the observed increased
273 ribosome levels of the Δ*ymcA* strain already without heat shock (time point 0 in **Fig. 5B**). After
274 15 minutes of heat shock, Δ*ymcA* shows 20% more aggregated proteins than WT. The
275 (p)ppGpp^0 Δ*ymcA* mutant exhibits even higher protein aggregation than Δ*ymcA* or (p)ppGpp^0
276 strains alone, further supporting that (p)ppGpp and the Y-complex act independently on the
277 regulation of ribosome levels and translation (**Supplementary Fig. 8C**). Mutants of the Y-
278 complex are also strongly affected by other proteotoxic stresses, such as osmotic and oxidative
279 stress, but not by ethanol (**Supplementary Fig. 8D**), which further demonstrates the
280 importance of controlling ribosome levels under proteotoxic stress conditions.

281 We observed that the Y-complex globally controls the RNase Y-mediated maturation of
282 transcripts and is involved in adjusting ribosome levels to the growth state, allowing the
283 endonuclease RNase Y to initiate the processing and degradation of rRNA and r-protein
284 transcripts. The absence of the Y-complex results in an abundance of idle ribosomes, which
285 interfere with the downregulation of translation and increase sensitivity to protein folding
286 stresses.

287 **Discussion**

288 Bacterial adaptation to environmental challenges depends on their ability to quickly change
289 gene expression. Beyond the well-known regulation of transcription initiation, we observed
290 here that post-transcriptional mechanisms, which influence RNA stability or translation
291 efficiency, also contribute to the rapid and tailored cellular response. In this context, the control
292 of RNases plays a critical role, since we show that the fitness of *B. subtilis* during heat shock
293 is critically dependent on certain non-essential RNases and the Y-complex, which controls the
294 substrate selection of the quasi-essential endonuclease RNase Y[26] (**Fig. 1B-C**). Together, our
295 findings demonstrate that the Y-complex – RNase Y system is a regulatory hub that modulates
296 gene expression and the cell's translational capacity during stress response.

297 Our RNA-seq analyses reveal that the Y-complex may regulate transcripts involved in a wide
298 range of metabolic pathways, developmental processes, stress responses, and translation
299 (**Fig. 2G, Supplementary Fig. 4A-B, Supplementary Tables 2, 6-7**). RNA processing by the
300 Y-complex-guided RNase Y can create new transcript isoforms[26] or modify regulatory
301 elements such as UTRs[26,31](**Fig. 2F**, **Supplementary Fig. 3**), thereby tailoring gene
302 expression to specific growth conditions. This wide regulatory scope of the Y-complex could
303 explain the known pleiotropic phenotypes in these mutants, like decreased sporulation,
304 competence, and defective biofilm formation[39–41].

305 Among these diverse functions in RNA processing, we discovered that the Y-complex initiates
306 ribosome degradation at the end of exponential growth by directing RNase Y to cleave 23S
307 and 16S rRNA (**Fig. 3A-B**, **Supplementary Fig. 7A-B**), thereby decreasing the levels of
308 ribosomes. This finding is consistent with previous suggestions that RNase Y can degrade
309 rRNA in aging *B. subtilis* spores[42].

310 The exact nature of how the Y-complex (YmcA, YlbF, and YaaT) associates with RNase Y is
311 an active subject of research. Recent evidence indicates that YmcA and YlbF transfer YaaT to
312 RNase Y, forming a stable, membrane-localized YaaT-RNase Y complex[35]. However, the
313 deletion of any of the Y-complex members leads to a strong decrease in the processing of
314 target mRNA[26], indicating that all Y-complex proteins are equally indispensable for RNA
315 processing. Based on the dynamic localization of YmcA and YlbF between the cell membrane
316 and the cytosol[43], we propose that these Y-proteins may also recognize substrates, including
317 ribosomes, and direct them to RNase Y for cleavage.

318 The two $[4Fe\text{-}4S]^{+2}$ clusters in the Y-complex[44] likely act as sensors for cellular growth, energy,
319 and stress, affecting how the complex controls RNase Y. This regulatory complex is localized
320 at the cell membrane, where RNase Y forms a dynamic degradosome-like network with other
321 RNases, helicases, and glycolytic enzymes[45–47]. This spatial co-localization may enable a
322 sequential degradation process: the Y-complex-guided RNase Y performs initial cleavage on
323 targets like rRNA, making fragments susceptible to further degradation by exonucleases such
324 as PNPase, and RNase J as observed with YaaT pull-down experiments (**Supplementary Fig.
325 7B**). Here, we propose that the Y-complex targets ribosomes to RNase Y and probably other
326 members of the membrane-localized degradosome-like network (**Fig. 6**). This suggests
327 complex spatial control of RNA processing and ribosome decay, separate from transcription
328 and translation in the cytoplasm.

329 Most of the cleavages we observed in rRNA were in the 23S (**Fig. 3A**); however, the Y-complex
330 and RNase Y can also initiate 16S degradation in the late exponential phase and during heat
331 shock (**Fig. 3A**, **Supplementary Fig. 7A**, **Supplementary Fig. 8A**). Recently, it was observed
332 that the exoribonuclease RNase R alone can degrade 16S rRNA[48], suggesting that
333 endonucleolytic cleavages might not be strictly necessary for 16S degradation. Since RNase
334 R is induced as part of the general stress response[49], it suggests a possible stress-specific
335 and Y-complex-independent degradation pathway for 16S rRNA.

336 Complete ribosome decay requires the concurrent degradation of r-proteins (**Fig. 6**). These
337 proteins might be passively released from the ribosome into the cytoplasm during the
338 degradation of the rRNA. Since this would also change their interaction with rRNA, they might
339 misfold and aggregate, and can subsequently be degraded by AAA+ protease complexes.
340 Alternatively, these AAA+ protease complexes could be actively recruited to the site of

341 ribosome degradation to simultaneously extract and degrade the r-proteins along with rRNA.
342 AAA+ protease complexes such as ClpCP with McsB or the membrane-associated FtsH, which
343 functions in protein homeostasis in *B. subtilis*[50], could be involved in the proteolysis of the r-
344 proteins (**Supplementary Fig. 7B**).

345 Strikingly, the Y-complex additionally processes transcripts encoding r-proteins and other
346 translation factors (**Fig. 2G**), such as BipA, EF-Tu, and EF-G (**Supplementary Fig. 3E-F**),
347 potentially regulating their translation or leading to their decay. This is supported by the findings
348 that the Y-complex is necessary to process some r-protein transcripts at the mid-logarithmic
349 phase[26], and RNase Y depletion in this growth phase leads to an increased abundance of
350 transcripts of r-proteins, such as *rplS, rpsO, rpmA, rpsD, rpsB,* and *rplU*[51].

351 The control of translation is an important component of many stress response mechanisms.
352 During nutrient starvation, downregulating translation allows the reallocation of resources to
353 biosynthetic pathways[52]. During proteotoxic stresses, it could relieve the overwhelmed PQC
354 system by reducing the synthesis of new proteins that could potentially aggregate[53]. The stress
355 transcription factor Spx and the alarmones (p)ppGpp regulate ribosome levels in *B. subtilis*,
356 and the lack of both impairs growth at 50°C[7]. Our work establishes a mechanistic link between
357 the regulation of ribosome levels through synthesis and decay. The severe growth defect
358 observed in cells lacking both (p)ppGpp and the Y-complex indicates that both of these
359 systems are important for transitioning from exponential to stationary phase. Furthermore, the
360 absence of their combined regulation of translation results in elevated ribosome levels and
361 increased accumulation of protein aggregates. (**Supplementary Fig. 8C**). In times of nutrient
362 limitation, the collective function of (p)ppGpp and the Y-complex in regulating ribosome levels
363 by inhibiting their synthesis and initiating degradation allows resource allocation to other
364 biosynthetic pathways (**Fig. 6**).

365 These strategies are not exclusive to *B. subtilis*, as different organisms use various
366 mechanisms to degrade ribosomes. These must specifically recognize the ribosome or its
367 subunits to disassemble them and target rRNA and r-proteins for degradation. For example,
368 *E. coli* cells transitioning into the stationary phase also initiate ribosome degradation by the
369 membrane-associated endonuclease RNase E[54,55], which is functionally equivalent to RNase
370 Y in *B. subtilis*[56]. RNase E forms the scaffold of the membrane-associated degradosome
371 network in *E. coli*[57]. This could allow for the combined activity of endo- and exonucleases,
372 facilitating the complete degradation of the ribosome[56,58]. In addition, it was observed that *E.*
373 *coli* r-proteins are degraded by the Lon AAA+ protease during starvation[59]. In eukaryotic cells,
374 nutrient starvation also triggers ribosome degradation via the ubiquitin-proteasome system or
375 via specialized autophagy pathways, such as ribophagy[60]. Recent studies have described how
376 stress- or starvation-induced degradation of the 40S ribosome involves the ubiquitylation of

377 proteins S3 and S5. This allows RIOK3 binding, leading to the decay of 18S rRNA by unknown
378 RNases[61–63].

379 In summary, we identified the Y-complex as a key regulator of ribosome abundance in *B.*
380 *subtilis*. The Y-complex regulates the translational activity by triggering ribosome decay and
381 processing transcripts for new ribosomal components. Our findings contribute to the
382 understanding of ribosome degradation by identifying a direct pathway and illustrating how this
383 process is integrated with other stress response mechanisms to control cellular growth and
384 survival. Further studies are required to understand the molecular signals that trigger ribosome
385 degradation and how the decay of rRNA and r-proteins is temporarily and spatially coordinated.

386

387 **Materials and methods**

388 Growth conditions

389 Unless stated the contrary, strains (**Supplementary Table 10**) were streaked on LB plates (5
390 g/l yeast extract, 10 g/l tryptone agar, 10 g/l NaCl, 1.5% agar) containing the required
391 antibiotics for selection (1 µg/ml erythromycin + 25 µg/ml lincomycin, 150 µg/ml spectinomycin
392 or 10 µg/ml kanamycin) and incubated overnight at 37°C. A single colony was inoculated in 3
393 ml of LB medium and grown overnight at 37°C and 180 rpm, then used as the inoculum for
394 subsequent experiments.

395 Strain construction

396 For constructing the strains Δ*ymcA::erm*^{R} and Δ*yaaT::erm*^{R}, the loci containing the resistance
397 cassette were PCR-amplified from the respective strains of the BKE library[20] and transformed
398 in *B. subtilis* WT. The deletions of Δ*rel::kan*^{R} and Δ*ylbF::erm*^{R} were constructed as described
399 in Ref.[20]. For promoter activity reporter strains, the *gfp*(mut2) gene was cloned downstream of
400 the promoters of interest, using the integrative plasmid pDR111 as a backbone.

401 For transformation, 600 µl of an overnight culture of the receptor strains were diluted in 5 ml
402 competence medium (17.5 g/l K_2HPO_4, 7.5 g/l KH_2PO_4, 2.5 g/l $(NH_4)_2SO_4$, 1.25 g/l tri-sodium
403 citrate x2 H_2O, 0.5% glucose, 7 mM $MgSO_4$, 0.1 mg/ml L-tryptophan, 0.02% casamino acids,
404 0.22 g/ml ammonium iron citrate) and grown at 37°C, 180 rpm, for 3 hours. Subsequently, 5
405 ml of starvation medium (17.5 g/l K_2HPO_4, 7.5 g/l KH_2PO_4, 2.5 g/l $(NH_4)_2SO_4$, 1.25 g/l tri-sodium
406 citrate x2 H_2O, 0.5% glucose, 7 mM $MgSO_4$) were added and grown for 2 more hours. One ml
407 of this culture was incubated with the DNA to be transformed and grown for 2 hours at 37°C
408 and 180 rpm. Positive clones were selected on LB agar containing the required antibiotics.
409 Genetic modifications were verified using PCR and DNA sequencing.

410 Genetic screening during heat shock

411 The BKE library[20] was replicated on LB agar plates containing 1 µg/ml erythromycin. Liquid
412 cultures were prepared in 200 µl LB medium supplemented with 1 µg/ml erythromycin and
413 grown for 42 hours at 30°C 200 rpm. All mutant strains were pooled and mixed for 15 minutes
414 using a magnetic stirrer. The pooled culture was centrifuged at 5000 rpm for 10 minutes at
415 18°C. The pellet was resuspended in LB medium to an OD_{600} of 65 and mixed with an equal
416 volume of 50% glycerol. The pooled library was aliquoted and kept at -80°C.

417 For each replicate, a tube of the pooled library was quickly unfrozen in a water bath at 30°C
418 and used to inoculate 75 ml LB medium in 500 ml flasks to a starting of OD_{600} 0.05. The culture
419 was grown in a water bath at 30°C, 180 rpm, until OD_{600} 0.4. Fifty ml of culture were split into
420 two 250 ml flasks. One flask was transferred to 50°C, 180 rpm for heat shock. The other flask

421 was used as a control sample and was kept at 30°C. One ml samples were collected for gDNA
422 purification at 0 and 2 hours post temperature shift. Samples were pelleted for 2 minutes at
423 13,000 rpm and washed once with 500 µl PBS. gDNA was purified using the Wizard® Genomic
424 DNA Purification Kit (Promega, A1120) and stored at -20°C until further processing.

425 The strain-specific barcodes were amplified using indexed primers (**Supplementary Table 7**)
426 with the Collibri Library Amplification Master Mix (ThermoFisher, A38539050) according to the
427 manufacturer's instructions, with 100 ng of gDNA as input, for 22 cycles. Barcodes were gel-
428 purified, quantified, pooled equimolarly, and sequenced using the Illumina NovaSeq2 single-
429 read method at the Sequencing Core Facility of the Max Planck Institute for Molecular Genetics
430 (Berlin, Germany).

431 To calculate the fitness score of each deletion mutant from barcode abundance, BEAN-counter
432 v2.6.1[64] was used with the following settings. A fixed amplicon read structure was used with
433 an index at position 0, the common primer sequence GCAGGCGAGAAAGGAGAG at position
434 9, and the mutant barcode at position 27 of read 1. All other settings were used with default
435 values. The sample before heat shock served as a reference to which all other time points
436 were compared. All comparisons were performed with three biological replicates.

437 Fitness data was further analyzed using the R statistical computing language (v4.3.3). For
438 annotation, protein-related information was fetched using the Uniprot REST API (29 February
439 2024). Average fitness per gene, condition, and time point was calculated as the arithmetic
440 mean of the fitness score from three biological replicates. Differential fitness ΔF, e.g. for
441 comparison of treatment *versus* control at a particular time point, was calculated as $\Delta F =$
442 $F_{treatment} - F_{control}$. A two-sided Student's t-test was performed to evaluate statistical significance
443 for each gene, and the obtained *p*-value was corrected using the Benjamini-Hochberg
444 procedure[65].

445 Growth curves

446 Twenty-five ml of LB medium were inoculated with an overnight culture to a starting OD_{600} 0.05
447 in 250 ml Erlenmeyer flasks. Cultures were grown at 37°C 180 rpm in a water bath. OD_{600} was
448 monitored every 30 minutes. The average and standard deviation of three biological replicates
449 were calculated.

450 Heat shock survival

451 Cultures were inoculated in 25 ml LB medium to OD_{600} 0.05 and incubated in a water bath at
452 37°C 180 rpm. At OD_{600} 0.3 – 0.4, the cultures were exposed to a heat shock at 54°C for 2
453 hours, and samples for viability measurement were obtained every 30 minutes. Viability was
454 measured by spotting 4 µl of 1:10 serial dilutions in PBS of each sample on LB agar. The plates

455 were incubated overnight at 30°C, and the colony-forming units (CFU) were counted. The
456 CFU/ml was calculated for each sample, and relative viability was determined using samples
457 before heat shock as a reference.

458 Isolation of protein aggregates

459 Twenty-five ml of culture were harvested before and 15 minutes after heat shock at 54°C by
460 centrifugation for 5 minutes at 10,000 rpm. The pellets were washed once with buffer A (100
461 mM HEPES pH 8.0, 150 mM NaCl) and lysed by bead-beating in buffer B (100 mM HEPES
462 pH 8.0, 150 mM NaCl, cOmplete EDTA-free protease inhibitor) using 0.1 mm glass beads.
463 Afterwards, samples were centrifuged at 1000 x *g* for 2 minutes to obtain the cell extract. The
464 soluble fraction was separated from protein aggregates by centrifugation for 15 minutes at
465 11,000 x *g* at 4°C. To remove membrane proteins, the aggregates were resuspended in buffer
466 B containing 1% Triton X-100 and incubated for 1 hour at 4°C. Protein aggregates were
467 recovered by centrifugation at 11,000 x *g*, 4°C for 15 minutes and resuspended and incubated
468 as described above. Protein aggregates were washed again with buffer B + 0.5% Triton X-
469 100, and the detergent was removed in a final wash using buffer B. Pellets containing protein
470 aggregates were resuspended in buffer B + 2% SDS by boiling for 5 minutes at 95°C. Protein
471 concentration was measured using the Rapid Gold BCA Protein-Assay-Kit (Pierce™, A53225).
472 The percentage of aggregated protein was calculated to the total protein content in the cell
473 extract.

474 Spot test

475 Overnight cultures were diluted 1:1000 in LB medium without antibiotics and incubated at 37°C
476 180 rpm for 7-8 hours. The cultures were diluted to OD_{600} 1 in fresh LB medium in a 96-well
477 plate. Seven serial 1:10 dilutions were prepared in 1x PBS. Four µl of each dilution was spotted
478 on LB agar containing different stressors (concentration indicated in the figures). Plates were
479 freshly prepared before use.

480 RNA purification

481 Samples for RNA purification were collected at the indicated time points: exponential phase
482 (OD_{600} ~ 0.3), late exponential phase (OD_{600} ~ 1) and transition phase (100 minutes after late
483 exponential phase). Rifampicin was added to a final concentration of 100 µg/ml for 10 minutes.

484 Samples were harvested by mixing with the same volume of cold 1:1 acetone:ethanol and
485 centrifugated at 9,000 rpm for 5 minutes, 4°C. RNA purification was performed according to
486 Ref.[27] with slight modifications: The pellet was washed twice in 1 ml TE-sucrose buffer (50 mM
487 Tris-HCl pH 8.0, 10 mM EDTA, 25% sucrose) and centrifugated at 10,000 rpm for 5 minutes,
488 4°C. Cells were resuspended in 130 µl lysis buffer (20 mM Tris-HCl pH 8.0, 50 mM EDTA, 20
489 % sucrose) supplemented with 3.2 mg/ml lysozyme and incubated on ice for 5 minutes. Two

490 hundred µl of lysis executioner (2% SDS, 1 mg/ml Proteinase K) were added to the samples
491 and incubated at 95°C for 1.5 minutes. Samples were mixed with 1 ml of TRIzol (Ambion) and
492 incubated at room temperature. After 5 minutes, 250 µl chloroform was added to each sample
493 and mixed by vortexing. After 10 minutes at room temperature, the samples were centrifuged
494 for 10 minutes at 11,000 rpm. The RNA was isopropanol-precipitated at -20°C overnight. RNA
495 was pelleted at 11,000 rpm for 20 minutes at 4°C, washed with 1 ml 70% ethanol followed by
496 another centrifugation at 13,000 rpm for 10 minutes at 4°C. The pellet was air-dried and
497 resuspended in 50 µl nuclease-free water.

498 ISCP RNA sequencing

499 RNA sequencing was performed as previously described[66]. In brief, total RNA was treated with
500 TURBO DNase (Ambion, AM2238), depleted of ribosomal RNA using the riboPOOL rRNA
501 depletion kit for *B. subtilis* (siTOOLS; two reactions with 4.5 µg each) and purified using the
502 RNA Clean & Concentrator-5 kit (RCC-5; Zymo Research). RNA 5' triphosphates were
503 converted to monophosphates using RppH (NEB), and RNA was recovered using
504 phenol:chloroform:isoamyl alcohol extraction followed by ethanol precipitation. RNA ends were
505 repaired using T4 Polynucleotide Kinase (Thermo Scientific), before RNA was purified using
506 the RCC-5 kit and fragmented using an M220 Focused-ultrasonicator (Covaris) as described
507 by the manufacturer but with a treatment time of 100 s (microTUBE AFA Fiber Snap-Cap). After
508 purification using the RCC-5 kit, sequencing libraries were prepared from the recovered RNA
509 using the NEXTflex Small RNA-Seq Kit v3 (Bioo Scientific) according to the manufacturer's
510 protocol (including step G). Libraries were purified as described in step I of the NEXTflex Rapid
511 Directional qRNA-Seq Kit (Bioo Scientific) using Agencourt AMPure XP Beads (Beckman
512 Coulter; 0.9x bead-to-sample ratio). Sequencing was performed on an Illumina NovaSeq 6000
513 in paired-end mode with a read length of 100 bp at the Sequencing Core Facility of the Max
514 Planck Institute for Molecular Genetics (Berlin, Germany).

515 Processing of RNA sequencing data

516 FastQC (v0.11.5) was used to assess the quality of the data. Reads were filtered with a
517 minimum quality score of 10 and a length of at least 18 nt, cleaned from adapter sequences
518 using Cutadapt (v3.5)[67], and mapped against the *B. subtilis* reference genome (NC_000964.3)
519 using STAR (v2.7.10a_alpha_220314)[68] in 'random best' and 'end to end' modes. Resulting
520 BAM files were sorted and indexed with Samtools (v1.9)[69], and PCR duplication artefacts were
521 removed using UMI Tools (v1.1.0)[70]. Gene counts of annotated RefSeq genes were
522 determined with featureCounts (v2.0.3)[71] and differentially expressed genes (DEG) were
523 calculated with three replicates per condition and time point using DESeq2 (v1.24.0)[72]. *p*-
524 values were corrected for multiple testing using the Benjamini-Hochberg method[65]. To call

525 DEGs, a threshold of adjusted *p*-value < 0.05 and absolute log2 fold change > 1 was used.
526 Genome coverage profiles (total, 5' and 3' ends) were generated using a custom script utilizing
527 the HTSeq library (v2.0.2)[73]. We performed the aforementioned analysis steps using a
528 customized pipeline implemented in Snakemake (v7.14.0)[74].

529 Identification of Y complex cleavage sites

530 The Y-complex-dependent cleavage positions were identified following the previously
531 published procedure[66]. In brief, the genome coverage data was prefiltered with a count per
532 million (cpm) value ≥0.05, and only the RNA ends displaying a cpm ≥ 5 were further analyzed.
533 We carried out differential expression analysis of normalized 5′ and 3′ read ends by comparing
534 WT vs. Δ*ymcA* at the late exponential and transition phase. Y-complex-dependent ends were
535 identified using edgeR (v3.28.0)[75] with absolute log2 fold change ≥ 1 and FDR < 0.05, and kept
536 only if present in both comparisons. These results were further filtered with additional
537 parameters, i.e., the "proportion of ends (cleavage ratio)" and the "ratio of WT and Δ*ymcA*
538 proportion of ends" as was previously described[66]. Moreover, to reduce the potential set of
539 false positive processing sites even further, we applied an additional cut-off on the "proportion
540 of ends" parameter, i.e., we kept only processing sites with a cleavage ratio of the reference
541 strain (WT) ≥ 95%-percentile of the cleavage ratio of the mutant strain.

542 Impact of processing sites on transcript and operon expression

543 To examine the impact of cleavage sites on transcript and operon expression, as well as other
544 genomic features such as untranslated regions (UTRs) and regulatory elements, we calculated
545 transcript per million (TPM) values from variance-stabilized data for each annotated RefSeq
546 gene (transcript level) and for each operon as defined in the BSGatlas (v1.1)[76] using the
547 DESeq2 package and a custom Python script. Furthermore, all Y-complex-dependent
548 cleavage sites were mapped to various genomic features, including coding regions, UTRs,
549 terminator regions, and riboswitches, as defined in the BSGatlas[76] (**Supplementary Table 2**).

550 Processing site sequence logo

551 The sequence logos were generated with Logomaker (v0.8)[77], specifically for 5' and 3' end U-
552 type cleavage sites. For this, we extracted 30 nt sequences centered at the cleavage site and
553 calculated the logos with a GC content of 43.5%.

554 RNA secondary structure prediction

555 The RNA structure surrounding Y-complex-dependent cleavage sites was estimated by
556 calculating the MFE (ΔG in kcal/mol) utilizing RNAfold (v2.6.4)[78]. This analysis employed a
557 sliding window approach with 50 nt sequences, focusing on a 200 nt region centered around
558 the position of interest. The average MFE at each nucleotide was then calculated. To calculate

559 and visualize the background folding energy, we randomly draw potential processing sites from
560 the genome determined with the corresponding 5' or 3' end motif and calculate the average
561 MFE at each nucleotide as described above. Potential processing sites were drawn 50 times
562 independently.

563 Overrepresentation analysis

564 Annotations of operons were obtained from BSGatlas[76] and gene categories from Subtiwiki
565 (24 July 2023)[79]. The overrepresentation analysis was performed using the R statistical
566 computing language (v.4.2.2) and the Bioconductor package Category (v.2.64.0).

567 Northern blot

568 Biotinylated RNA probes were prepared using the HighYield T7 Biotin11 RNA Labeling Kit
569 (UTP-based) (Jena Bioscience, RNT-101-BIOX) from PCR amplified fragments containing the
570 promoter for the T7 RNA polymerase (**Supplementary Table 11**). Probes were purified using
571 the Monarch® Spin RNA Cleanup Kit (NEB, T2040) according to the manufacturer's
572 instructions. Probes were designed taking into consideration the predicted cleavage sites.

573 One and a half µg of total RNA was separated on denaturing agarose gels (1% agarose,
574 20 mM MOPS, 5 mM NaOAc, 1 mM EDTA, 6.6% formaldehyde, pH 7.0) in 1x AGE-NB
575 Running Buffer (20 mM MOPS, 5 mM NaOAc, 1 mM EDTA, 0.74% formaldehyde, pH 7.0).
576 The gel was washed 3 times with milli-Q water and once with 10x SSC buffer, and the
577 nitrocellulose membrane was washed once with milli-Q water and once with 10x SSC. The
578 RNA was transferred using a vacuum blotter at 300 mbar covered with 10x SSC for 1.5 hours.
579 After transfer, the membrane was washed for 2 minutes with 6x SSC, once with water, and
580 dried and crosslinked at 254 nm 0.12 J twice. The membrane was developed with methylene
581 blue, and the staining was removed by washing with 0.2x SSC containing 1% SDS, followed
582 by washing with milli-Q water. The hybridization of 16S or 23S rRNA probes was performed
583 using the North2South Chemiluminescent Hybridization and Detection Kit (Thermo) and
584 North2South Hybridization Stringency Wash Buffer (2X) according to the manufacturer's
585 instructions. Blots were developed in a Vilber imaging system.

586 RT-qPCR

587 Twenty µg of total RNA were treated with TURBO DNase (Ambion, AM2238) and purified using
588 the Monarch® Spin RNA Cleanup Kit (NEB, T2040). Subsequently, cDNA was prepared using
589 the LunaScript RT Mastermix (NEB, E3025) and 2.5 µg of DNase-treated RNA as input.
590 Quantitative PCR was performed using the Luna Universal qPCR Master Mix (NEB, M3003)
591 in a QuantStudio 5 Real-Time PCR System (Applied Biosystems). To calculate changes in *gfp*
592 transcription, samples from the late exponential and transition phases were compared to those

593 from the exponential phase, with *pcp* serving as a reference gene using the Pfaffl method[80].
594 Primers used for RT-qPCR are listed in **Supplementary Table 11**.

595 Ribosome sedimentation in sucrose gradients

596 Cultures of WT and Δ*ymcA* were grown until the exponential phase (OD_{600} ~ 0.3), late
597 exponential (OD_{600} ~ 1), and transition phase (100 minutes after the late exponential phase).
598 Chloramphenicol was added at a concentration of 100 µg/ml 2 minutes prior to sample
599 collection. Fifty ml of culture were pelleted at 4,500 rpm for 10 minutes at room temperature.
600 Pellets were transferred to ice and resuspended in 2 ml of lysis buffer (20 mM Tris-HCl pH 8.0,
601 100 mM NH_4Cl, 10 mM $MgCl_2$, 0.4% Triton X-100, 0.4% NP-40, 1 mM chloramphenicol, 100
602 U/µl DNase I), and flash-frozen. Cells were lysed under cryogenic conditions using 5 cycles of
603 mix-milling at 30 Hz for 1 minute. Lysates (240 µg RNA) were laid over a 10-50% sucrose
604 gradient in 20 mM Tris-HCl pH 8.0, 100 mM NH_4Cl, 10 mM $MgCl_2$, 0.5 mM DTT and resolved
605 at 35,000 rpm for 3 hours at 4°C. Gradients were analyzed using a piston fractionator (Biocomp
606 instruments), and absorbance at 260 and 280 nm was monitored.

607 Pulldown of YaaT

608 Cultures of in-locus C-terminal FLAG-tagged *yaaT* strain were grown until the late exponential
609 phase (OD600 ~ 1). Two hundred ml of culture were pelleted at 15,000 rpm for 2 min. Pellets
610 were transferred to ice and resuspended in 1 ml of resuspension buffer (20 mM HEPES-KOH
611 pH 7.5, 30 mM NH_4Cl, 6 mM Mg-Acetate, 0.5 mM TCEP) supplemented with cOmplete EDTA-
612 free protease inhibitor), and flash-frozen. Cells were lysed under cryogenic conditions using 3
613 cycles of mix-milling at 30 Hz for 1 minute. Lysates were stored at -80°C until further
614 processing. Lysates were quickly melted at 30°C, incubated for 10 min on ice with RNase-free
615 DNase I (Roche), and clarified by centrifugation at 12,000 rpm for 5 min at 4°C. DDM (n-
616 dodecyl β-D-maltoside) was added to a 200 µM final concentration. The lysate (input sample)
617 was incubated with 200 µL of anti-FLAG M2 affinity gel (A2220, Sigma) for 2 h at 4°C with
618 constant shaking. Beads were washed 5 times with resuspension buffer supplemented with
619 200 µM DDM. Proteins were eluted for 45 min in resuspension buffer supplemented with 200
620 µM DDM and 150 µg/ml of 3x FLAG peptide (Sigma) at 4°C with constant shaking. Proteins
621 were identified and quantified using DIA-MS.

622 Sample preparation for MS-based proteomics

623 Samples were collected at the indicated time points: late exponential phase (OD_{600} ~ 1) and
624 transition phase (100 minutes after the late exponential phase). For the proteomic changes
625 during heat shock, cultures were grown at 37°C until OD_{600} ~ 0.3 and shifted to 54°C. Samples
626 were collected at 0, 15, 30, and 60 minutes after heat shock. Ten ml of culture were collected

627 by centrifugation at 4,500 rpm for 10 minutes, and the pellet was stored at -80°C until further
628 processing.

629 Cell pellets were resuspended in 1 ml of cold PBS and centrifuged at 13,000 rpm for 5 minutes
630 at 4°C. The pellet was washed once more with PBS, resuspended in 150 µL of lysis buffer
631 (100 mM HEPES pH 8.0, 2% SDS, 20 mM TCEP, 60 mM CAA), and lysed using bead beating.
632 Cell debris was discarded by centrifuging at 13,000 rpm for 5 minutes at 4°C. The supernatant
633 was boiled at 95°C for 5 minutes, cooled down to room temperature, and the protein
634 concentration was estimated using the Rapid Gold BCA protein assay kit (Pierce). Samples
635 were flash-frozen in liquid nitrogen and stored at -80°C until further processing.

636 All samples were subjected to SP3 sample preparation[81] on an Agilent BRAVO liquid handling
637 robot. Ten µg of a 1:1 mixture of hydrophilic and hydrophobic carboxyl-coated paramagnetic
638 beads (SeraMag, #24152105050250 and #44152105050250, GE Healtcare) were added for
639 each µg of protein. Protein binding was induced by the addition of acetonitrile to a final
640 concentration of 50% (v/v). Samples were incubated at room temperature for 10 minutes. The
641 tubes were placed on a magnetic rack, and beads were allowed to settle for 3 minutes. The
642 supernatant was discarded, and beads were rinsed three times with 200 µL of 80% ethanol
643 without removing the tubes from the rack. Beads were resuspended in digestion buffer
644 containing 50 mM triethylammonium bicarbonate and both Trypsin (Serva) and Lys-C (Wako)
645 in a 1:50 enzyme-to-protein ratio. Protein digestion was performed for 14 hours at 37°C in a
646 PCR cycler. Afterward, the supernatant was recovered and dried down in a vacuum
647 concentrator.

648 Proteomics using Mass spectrometry

649 All samples obtained during the late exponential and transition phase were analyzed on an
650 Orbitrap Exploris (Thermo Scientific) equipped with a FAIMS Pro device and coupled to a 3000
651 RSLC nano UPLC (Thermo Scientific). Samples were loaded on a PepMap trap cartridge (300
652 µm i.d. x 5 mm, C18, Thermo) with 2% acetonitrile and 0.1% TFA at a flow rate of 20 µl/min.
653 Peptides were separated over a 50 cm analytical column (Picofrit, 360 µm O.D., 75 µm I.D.,
654 10 µm tip opening, non-coated, New Objective) that was packed in-house with Poroshell 120
655 EC-C18, 2.7 µm (Agilent). Solvent A consists of 0.1% formic acid in water. Elution was carried
656 out at a constant flow rate of 300 nl/min using a 60-minute method: 8-30% solvent B (0.1%
657 formic acid in 80% acetonitrile) within 23 minutes, 30-45% solvent B within 3 minutes, 45-98%
658 buffer B within 0.5 minutes, followed by column washing and equilibration. Data acquisition on
659 the Orbitrap Exploris was carried out using a data-dependent acquisition (**DDA**) method in
660 positive ion mode. MS survey scans were acquired from 375-1500 m/z in profile mode at a
661 resolution of 60,000. AGC target was set to 200% at a maximum injection time of 25 ms.
662 Peptides with charge states 2-6 were isolated within a window of 1.2 m/z and subjected to

663 HCD fragmentation at a normalized collision energy of 27%. The MS2 AGC target was set to
664 200%, allowing a maximum injection time of 22 ms. Product ions were detected in the Orbitrap
665 at a resolution of 15,000. Precursors were dynamically excluded for 20 s. The cycle time was
666 set to 1 s for each of the two FAIMS voltages of −45 and −65 V.

667 LC-MS/MS analysis of the heat shock samples was performed on an Ultimate 3000 UPLC
668 coupled to a Lumos hybrid mass spectrometer (Thermo Scientific). Peptides were loaded onto
669 a PepMap trap cartridge (300 µm i.d. x 5 mm, C18, Thermo) with 2% acetonitrile and 0.1%
670 TFA at a 20 µl/min flow rate. Peptides were separated over a 50 cm analytical column (Picofrit,
671 360 µm O.D., 75 µm I.D., 10 µm tip opening, non-coated, New Objective) that was packed in-
672 house with Poroshell 120 EC-C18, 2.7 µm (Agilent). Solvent A consists of 0.1% formic acid in
673 water. Elution was carried out at a constant flow rate of 250 nl/min using a 60-minute method:
674 8-30% solvent B (0.1% formic acid in 80% acetonitrile) within 23 minutes, 30-45% solvent B
675 within 3 minutes, 45-98% buffer B within 0.5 minutes, followed by column washing and
676 equilibration.

677 The mass spectrometer was operated in data-independent acquisition (**DIA**) and positive
678 ionization mode. MS1 full scans (375–1500 m/z) were acquired with a resolution of 60,000, a
679 normalized automatic gain control target value of 120%, and a maximum injection time set to
680 55 ms. Peptide fragmentation was performed using higher energy collision-induced
681 dissociation and a normalized collision energy of 30%. MS2 spectra were acquired with a
682 resolution of 30,000 (first mass 100 m/z) with 8 m/z DIA windows between 400 and 1200 m/z.
683 A normalized automatic gain control target value of 100%, and a maximum injection time of
684 54 ms.

685 For pulldown samples, proteins were processed following the SP3 protocol as described
686 above. Label-free DIA analyses of peptides were acquired over 120 min by an Orbitrap Exploris
687 480 (Thermo Scientific) coupled to a 3000 RSLC nano UPLC (Thermo Scientific). Samples
688 were loaded on a pepmap trap cartridge (300 µm i.d. x 5 mm, C18, Thermo) with 2%
689 acetonitrile, 0.1% TFA at a flow rate of 20 µL/min. Peptides were separated over a 25 cm
690 analytical column (PepSep C18, 75 µm I.D., 1.5 µm). Solvent A consists of 0.1% formic acid
691 in water. Elution was carried out at a constant flow rate of 250 nL/min within 120 minutes.
692 Initially, a two-step linear gradient was applied: 3-30% solvent B (0.1% formic acid in 80%
693 acetonitrile) within 70.5 minutes, 30-45% solvent B within 13 minutes, followed by column
694 washing and equilibration. The column was kept at a constant temperature of 50°C.

695 The MS was operated in DIA mode for single-injection quantitative measurements of individual
696 samples with the following settings: 60k MS1 resolution, MS1 scan range 375-1600 m/z, 15k
697 MS2 resolution, MS2 scan range 120-1600 m/z, Normalized AGC target of 1000%, maximum

698 injection time 54 ms, and fixed normalized collision energy of 30. 12 m/z precursor isolation
699 windows with optimized window placements from 400.4319 to 1210.8024 m/z.

700 Proteomics data analysis

701 For samples at the late exponential and transition phase, Raw files were processed with
702 MSFragger v3.5 using the default settings. Briefly, peak lists were extracted from raw files and
703 searched using a Uniprot *Bacillus subtilis* database (v220530, taxonomy ID 224308) and a
704 database containing sequences of common contaminants and decoys. Trypsin/P was set as
705 enzyme specificity, allowing a maximum of two missed cleavages. Peptide matches were
706 filtered to 1% FDR using PeptideProphet and Philosopher (v4.4.0).

707 For samples during heat shock, DIA-NN (DIA-NN v1.8.1) was employed for DIA data analysis.
708 The main DIA-NN report, "report.txt", was used for all calculations. Fasta file
709 (Bacillus_subtilis_Strain168_UP000001570.fasta) was digested with a maximum of one
710 missed cleavage. Peptide length was restricted from 7 to 30 peptides, and the precursor m/z
711 range was set from 300 to 1800. N-terminal methionine excision was enabled. Cysteine
712 carbamidomethylation was selected as a fixed modification, and methionine oxidation and N-
713 terminal acetylation as variable modifications. The maximum number of variable modifications
714 was set to two. All other parameters were at default settings, including the 1% precursor FDR
715 and enabled match between runs (MBR). The main DIA-NN report, "report.pg_matrix.tsv," was
716 used for all calculations.

717 For pulldown samples, raw data analysis was performed using Spectronaut® (Biognosys AG,
718 Zurich, Switzerland) version 19.7.250203.62635 in directDIA+ deep mode using a UniProt *B.*
719 *subtilis* database (v220530, taxonomy ID 224308). Methionine oxidation and Acetyl (Protein
720 N-term) were set as a variable, and carbamidomethylation on cysteine residues was used as
721 a static modification. The FDR for PSM-, peptide-, and protein-level was set to 0.01. All
722 tolerances were set to dynamic for pulsar searches.

723 The R statistical computing language was used for data processing (v4.4.1). The main
724 comparison of WT, Δ*ymcA*, (p)ppGpp^{0,} and (p)ppGpp^{0} Δ*ymcA* mutants was based on samples
725 from data-dependent acquisition (DDA) experiments. Raw peptide intensity values from label-
726 free quantitation were imported as tabular output from MSFragger. The MSstats package
727 (v4.12.1)[82] was used to convert raw intensities to an MSstats experiment. In this process,
728 peptide quantification data was $\log_2$-transformed, median-normalized, and summarized to
729 protein abundance. All features mapping to a protein were used for quantification, Tukey's
730 median polish was used as a summarization strategy, and missing values were imputed using
731 MSstats' default strategy. Feature abundance and inferred protein quantity were visually
732 inspected using profile plots. Experimental groups were compared using MSstats'

733 *groupComparison* function, and the similarity of conditions and replicates was inspected using
734 principal component analysis (PCA, function *prcomp*). For annotation, protein-related
735 information was fetched from Uniprot using the Uniprot REST API (14 June 2024). In addition
736 to the DDA experiments, a time series of WT and Δ*ymcA* mutants was obtained using data-
737 independent acquisition (DIA) proteomics. To quantify relative changes, the $\log_2$ fold change
738 of each time point was calculated using the zero time point as a reference. To quantify absolute
739 protein abundance for the ribosomal proteome sector, the coarse-graining strategy was used
740 as in Ref.[83,84]. Briefly, two protein sectors (groups) were created containing all annotated
741 proteins of ribosomal subunits. Raw MS1 intensities for all proteins of the respective group and
742 time points were summed up and divided by the total sum of protein intensities, yielding the
743 protein mass fraction per sector.

744 **Data availability**

745 Amplicon-seq and RNA-seq raw reads have been deposited at the European Nucleotide
746 Archive (ENA) under accession number PRJEB90661. Raw proteomic data have been
747 deposited at the PRIDE database under the accession number PXD065465 for DDA
748 proteomics of late exponential and transition phase samples. The DIA proteomics raw data
749 from the heat shock experiment can be accessed using the accession number PXD065462.

750 **Author contributions**

751 K.T., K.D., and F.A.C.; Conceptualization. K.D., F.A.C., K.T., R.A.-B., T.F.W., and K.A.:
752 Methodology. F.A.C., K.D., K.S., V.S., K.H., and F.K.: Investigation. K.D., F.A.C., R.A.-B., M.J.,
753 K.A., S.R., and K.T.: Formal analysis. F.A.C., K.D., R.A.-B., M.J.: Visualization. F.A.C., K.D.,
754 and K.T.: Writing – Original Draft. K.T. and E.C.: Funding acquisition. All authors: Writing –
755 Review & Editing.

756 **Acknowledgments**

757 We thank Gert Bange (Philipps-Universität Marburg) and Rainer Nikolay (Max Planck Institute
758 for Molecular Genetics) for critically reading the manuscript and providing valuable feedback.
759 This work was funded by the Deutsche Forschungsgemeinschaft (Tu106/8, SPP1879 for K.D.
760 and K.T., Leibniz Prize for E.C.) and the Max Planck Society (for E.C. and K.T.).

761

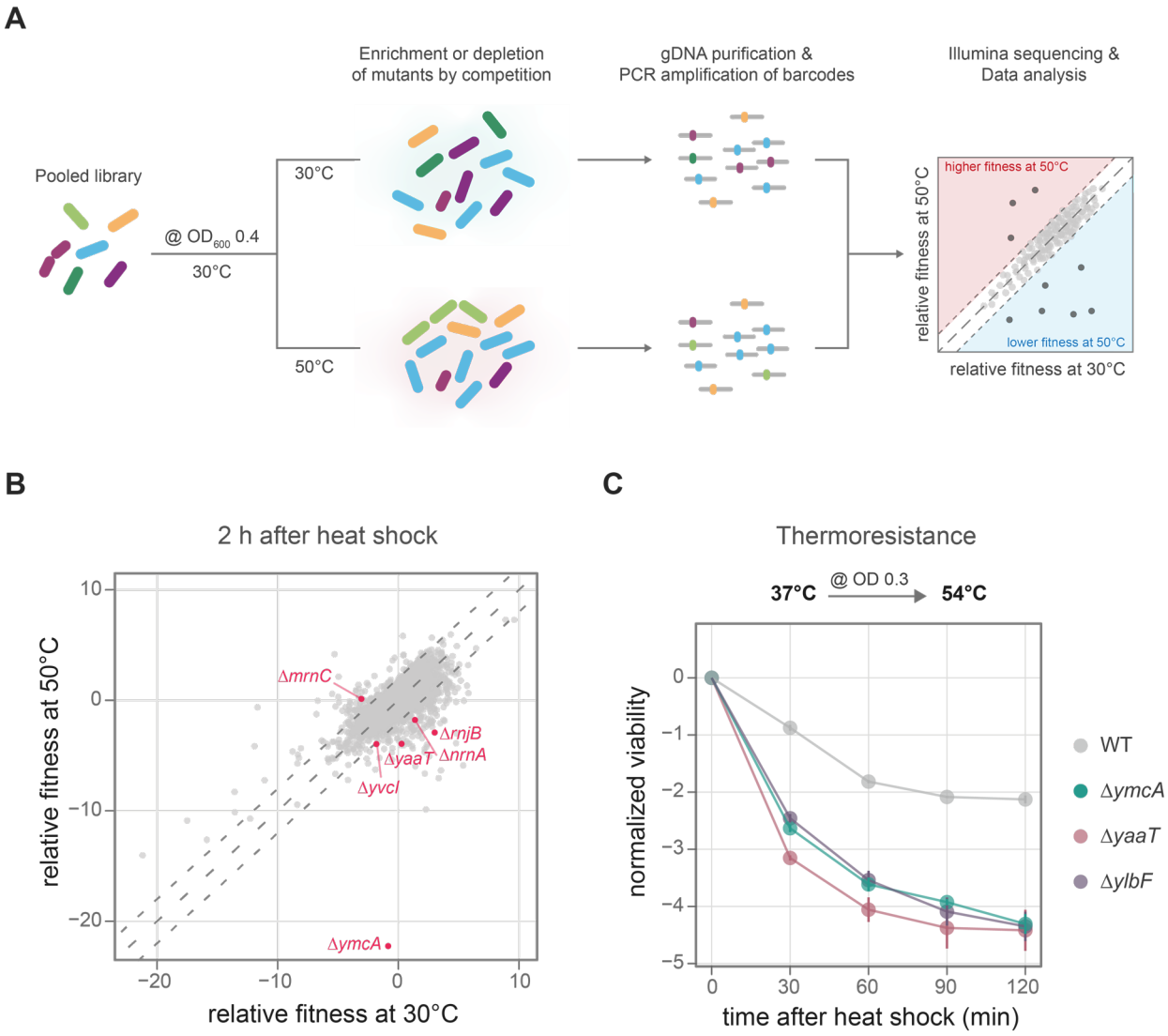

Figure 1. Genetic screening for genes involved in the heat shock response. A) Genetic screening experiment: the pooled library of deletion mutants (BKE) was grown at 30°C; when it reached an OD_{600nm} of 0.4, one fraction was exposed to 50°C while the other was maintained at 30°C. Genomic DNA (gDNA) was extracted from the library, and barcodes were amplified and sequenced using Next-Generation Sequencing. The fitness of each mutant at the mentioned temperatures and time points was calculated using BEANcounter. **B**) Relative fitness of each deletion mutant at 50°C (*y*-axis) and 30°C (*x*-axis) two hours post-temperature shift. Each point represents a deletion mutant, with mutants lacking RNase-related genes highlighted in magenta. The dotted lines indicate the range in which the relative fitness between the conditions differed by less than 2. Data represent the average of three biological replicates. A negative relative fitness value means that the abundance of the deletion mutant, compared to the rest of the population, was negatively affected by the treatment, while a positive value means an increased abundance in this condition. **C)** Changes in the viability (log_{10}CFU/ml) of WT and *ymcA, ylbF,* and *yaaT* deletion mutants to a severe heat shock at 54°C. Values were normalized to the viability at timepoint 0 min. The data represents the average ± standard error of three biological replicates.

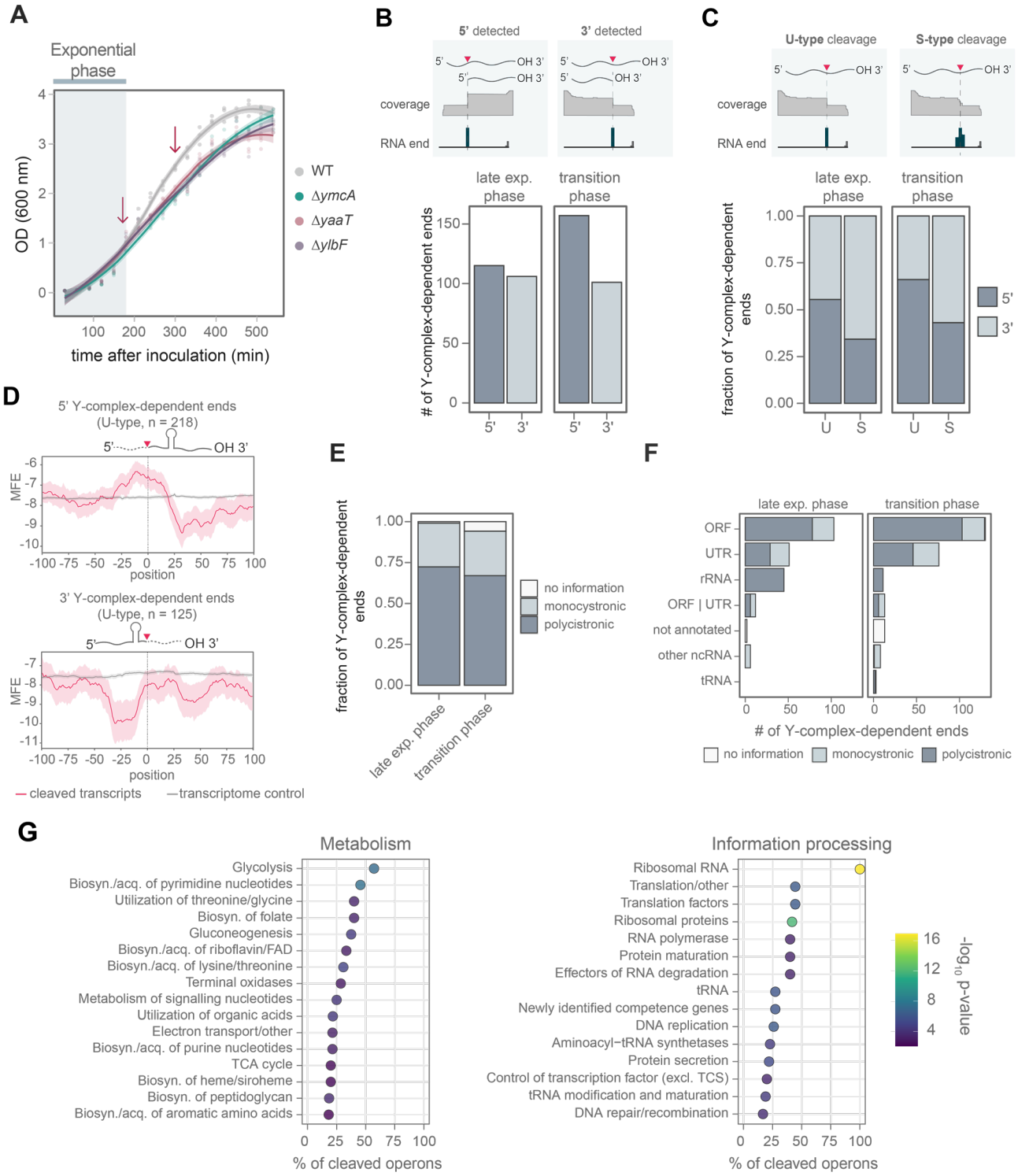

Figure 2. Identification of Y-complex-dependent cleavages at late exponential and transition phase. A) Growth curves of WT, *ymcA*, *ylbF*, and *yaaT* deletion mutants in LB at 37°C. The blue bar marks the exponential phase. Arrows indicate sample collection for the ISCP method at the late exponential and transition phases. Three biological replicates are displayed with a smooth curve regression. **B)** Number of RNA 3' or 5' ends identified at the two growth phases. **C)** Fraction of identified 3' or 5' ends displaying U-type (unique) or S-type (stepped) profiles. **D)** Minimum free energy (MFE) was calculated on 50 nt windows for RNAs cleaved by the Y-complex with U-type ends (in magenta). Transcripts that share the same cleavage motif but are not processed were used as a control (in gray). rRNA genes were excluded from the analysis since they are highly structured. **E)** Fractions of ends identified in genes transcribed in polycistronic or monocistronic RNA. **F)** Count of RNA features where

789 Y-complex-dependent ends are detected at either growth phase. Annotations were obtained from
790 BSGatlas[76]. **G)** Overrepresentation analysis of pathways whose transcripts are cleaved by the Y-
791 complex during the late exponential phase. Operons were assigned to be involved in a pathway if they
792 code for one gene participating in such a pathway. As genes in the same operon can have different
793 functions, transcripts may be linked to multiple roles. Pathway annotations were retrieved from
794 SubtiWiki[79]. The color indicates the statistical significance of the enrichment. Biosyn = biosynthesis, acq
795 = acquisition, excl TCS = excluding two-component systems.

796

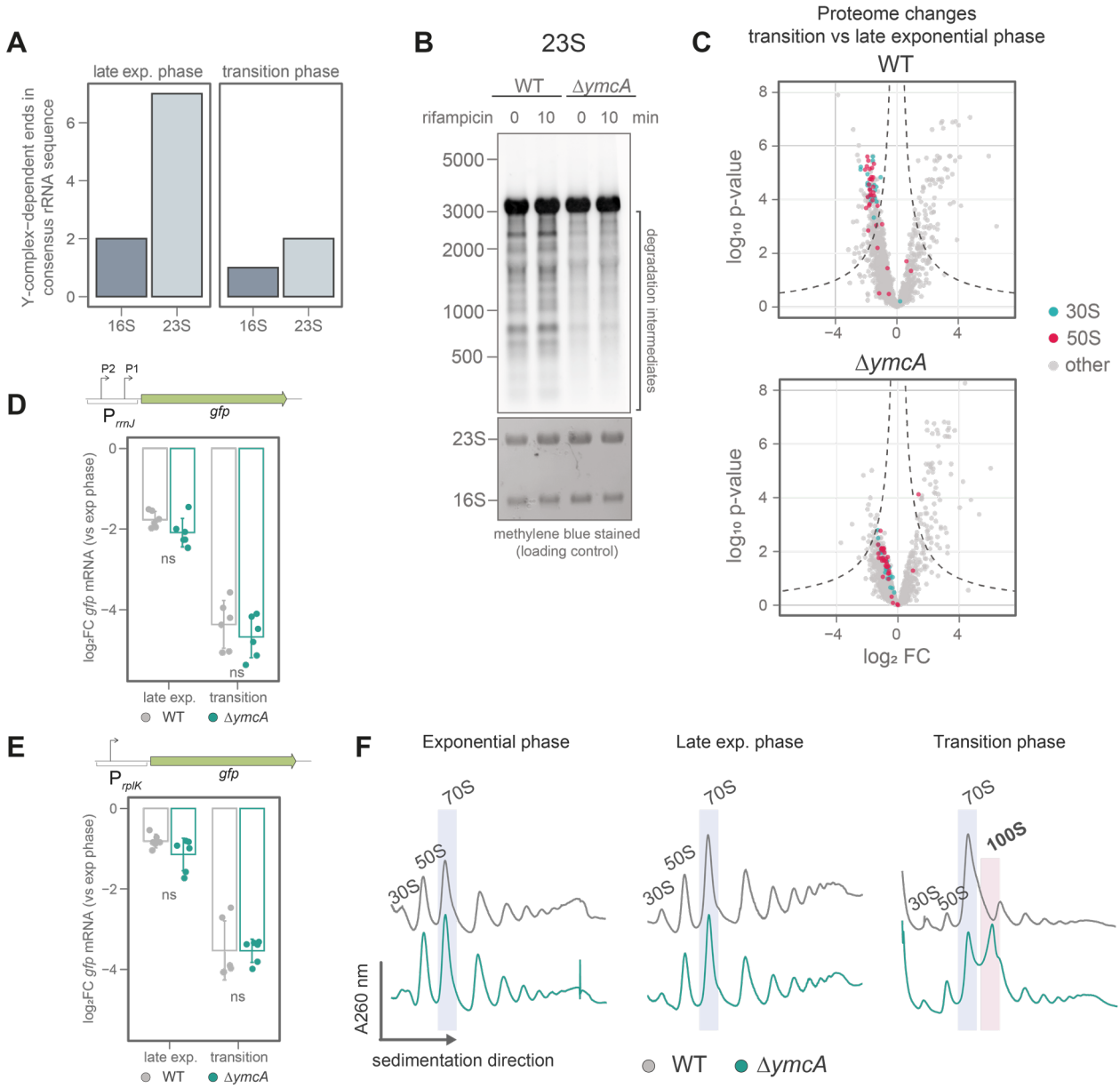

Figure 3. The Y-complex controls ribosome levels by initiating rRNA degradation. A) Number of cleavages detected by ISCP in *B. subtilis* rRNA during the late exponential and transition phase. **B)** Northern blot against 23S of WT and Δ*ymcA* cells at the late exponential phase, before and after treatment with 100 µg/ml rifampicin to stop transcription. The methylene blue-stained membrane is shown as a loading control. This image is representative of three biological replicates. **C)** Volcano plot of protein quantification of WT and Δ*ymcA* strains comparing transition to late exponential phase. The proteins composing the small (30S) and major (50S) ribosome subunits are highlighted in cyan and magenta, respectively. The data shows the average of four biological replicates. Activity of the promoter controlling **D)** *rrnJ* (rRNA) or **E)** the *rplK* (r-protein) transcription at late exponential and transition phase compared to the exponential phase in WT and Δ*ymcA*. The promoters were cloned controlling *gfp* transcription, which was measured using RT-qPCR. The *pcp* transcript was used as a reference. Individual values and the average ± standard deviation of three biological replicates and two technical replicates are shown. The statistical significance was tested using student's *t*-test. ns: *p*-value > 0.05. **F)** Ribosome sedimentation profile in 10-50% sucrose gradients of WT and Δ*ymcA* in exponential, late exponential, and transition phases. The 70S and 100S ribosomes are highlighted with a blue or red box, respectively. The data is representative of three biological replicates.

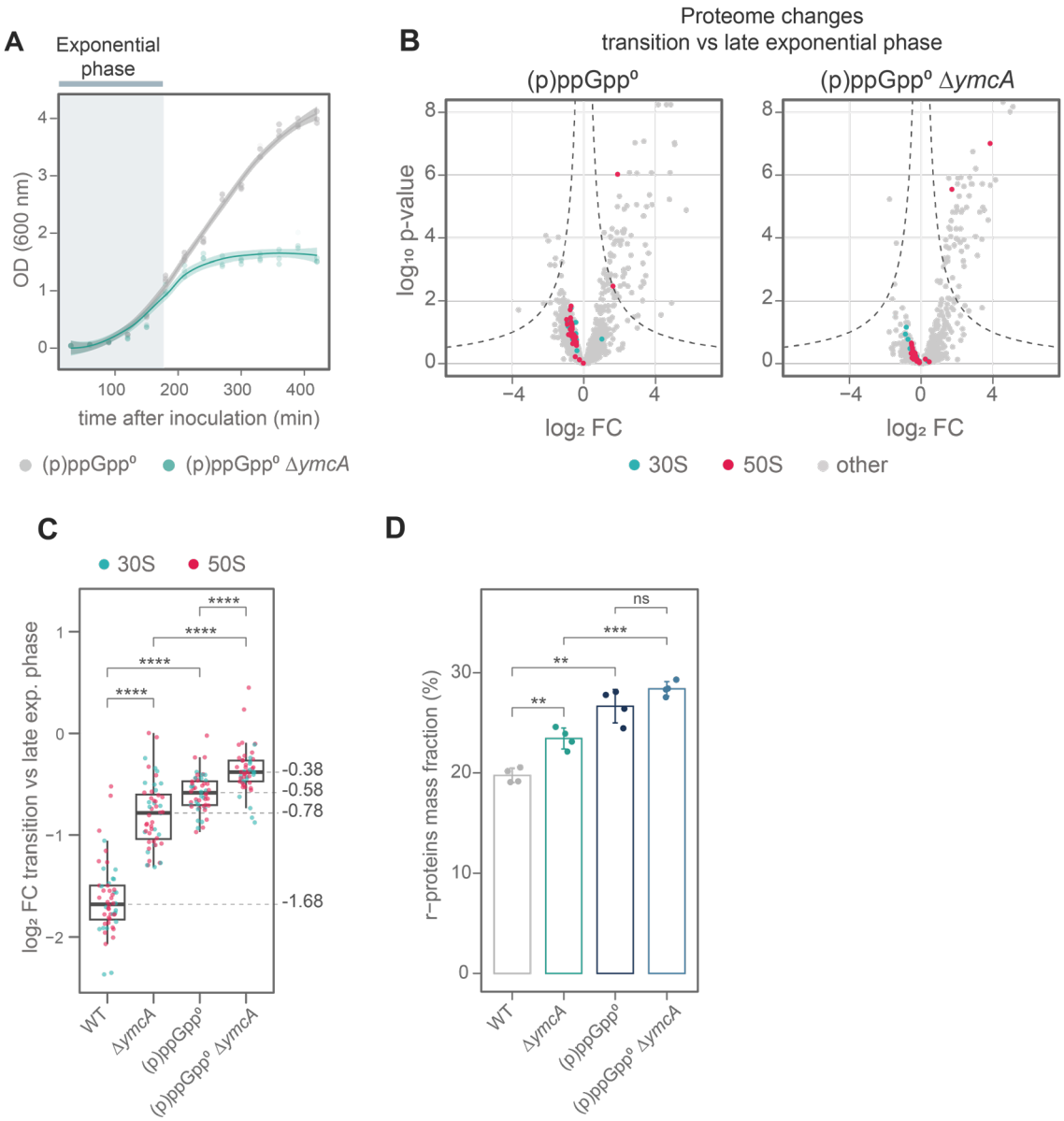

Figure 4. The alarmones (p)ppGpp and the Y-complex are important for controlling ribosome levels. A) Growth curve of (p)ppGpp^0 and (p)ppGpp^0 Δ*ymcA* strains in LB at 37°C. The blue bar marks the exponential phase. Three biological replicates are displayed with a smooth curve regression. **B)** Volcano plot of proteomic changes of (p)ppGpp^0 and (p)ppGpp^0 Δ*ymcA* cultures comparing transition to exponential phase. The proteins composing the small (30S) and major (50S) ribosome subunits are highlighted in cyan and magenta, respectively. The data shows the average of four biological replicates. **C)** Comparison of r-proteins downregulation in WT, Δ*ymcA,* (p)ppGpp^{0,} and (p)ppGpp^0 Δ*ymcA* during the transition phase compared to the late exponential phase. The boxplot represents the interquartile range (IQR) and the median in the center. Whiskers show the variability outside quartile 1 (Q1) and Q3 and were calculated as Q1-1.5*IQR and Q5+1.5*IQR, respectively. Proteins are highlighted like in **B**. Alternative r-proteins were excluded from the analysis. The statistical significance was tested using paired Wilcoxon test. ****: *p*-value ≤ 0.0001. **D)** Proteome fraction (in %) of r-proteins mass, measured by mass spectrometry. The r-protein mass fraction was calculated for the indicated strains. Individual values and the average ± standard deviation of three biological replicates are shown. The statistical significance was tested using student's *t*-test. ns: *p*-value > 0.05, **: *p*-value ≤ 0.01, ***: *p*-value ≤ 0.001.

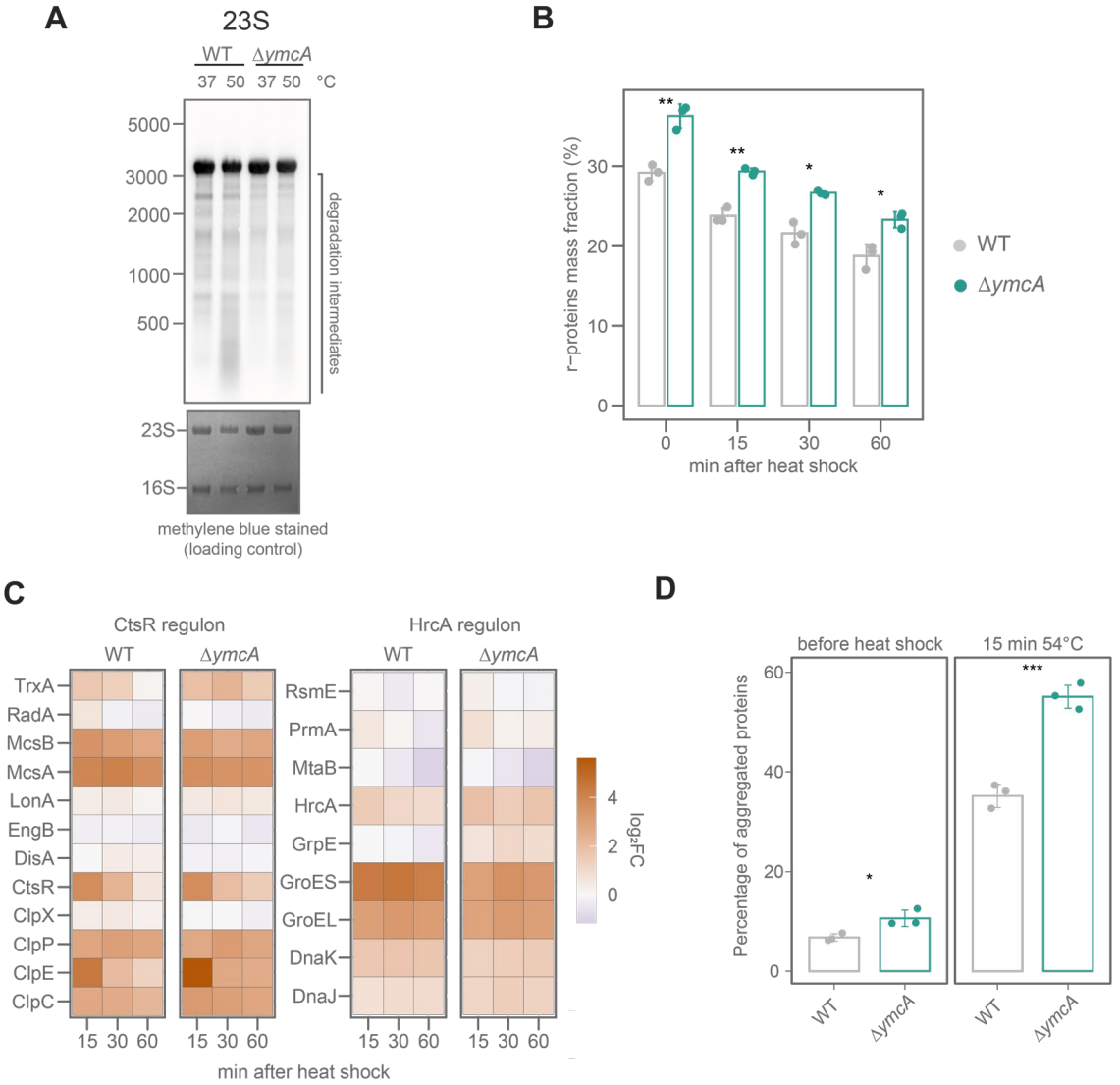

Figure 5. Control of ribosome levels and protein homeostasis in *ymcA* mutant during heat shock. **A)** Northern blot against 23S of WT and Δ*ymcA* cells at exponential phase before or after a heat shock. The methylene blue-stained membrane is shown as a loading control. This image is representative of three biological replicates. **B)** Proteome fraction (in %) of r-proteins mass, measured by mass spectrometry. Individual values and the average ± standard deviation of three biological replicates are shown. The statistical significance was tested using student's *t*-test. *: *p*-value ≤ 0.05, **: *p*-value ≤ 0.01. **C)** Induction of CtsR and HrcA regulons after heat shock (50°C) in WT and Δ*ymcA*. Proteins were measured by mass spectrometry. The color bar shows the $\log_2$ fold change compared to the control before heat shock. **D)** Percentage of aggregated proteins before and after a 15 min heat shock at 54°C in WT and Δ*ymcA*. Individual values and the average ± standard deviation of three biological replicates are shown. The statistical difference was tested using student's *t*-test. *: *p*-value ≤ 0.05, **: *p*-value ≤ 0.01, ***: *p*-value ≤ 0.001.

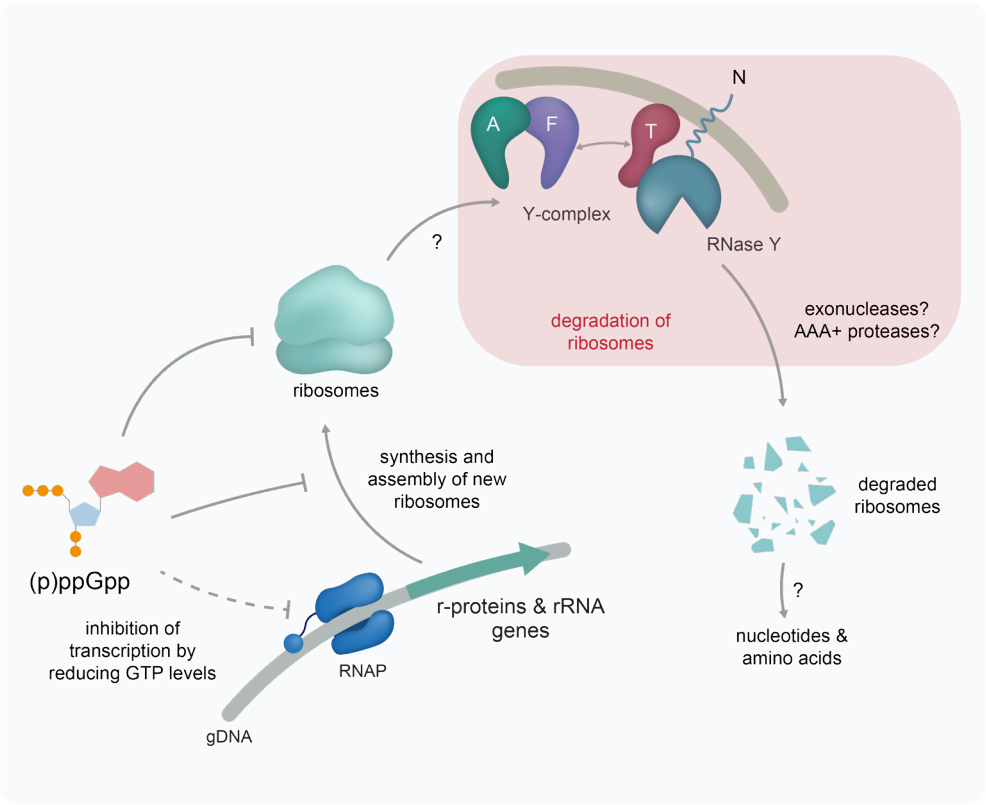

846

847 **Figure 6. Control of ribosome levels by (p)ppGpp and the Y-complex.** The alarmone (p)ppGpp
848 reduces the biogenesis of new ribosomes by indirectly inhibiting the transcription of rRNA and r-proteins
849 mRNA. (p)ppGpp inhibits GTPases that are involved in new ribosome assembly. Additionally, (p)ppGpp
850 reduces translation by binding to specific GTPases. The Y-complex can initiate the degradation of
851 ribosomes, which need to be transported to the membrane by unknown mechanisms. Exonucleases
852 and AAA+ protease complexes might assist in ribosome degradation for the complete degradation of
853 rRNA and r-proteins, which could partially replenish the nucleotide and amino acid pools during
854 starvation.

855

856 **References**

857 1. Hecker, M., Schumann, W. & Völker, U. Heat-shock and general stress response in *Bacillus*
858 *subtilis*. *Mol. Microbiol.* **19**, 417–428 (1996).
859 2. Mogk, A. *et al.* The GroE chaperonin machine is a major modulator of the CIRCE heat shock
860 regulon of *Bacillus subtilis*. *EMBO J.* **16**, 4579–4590 (1997).
861 3. Krüger, E. & Hecker, M. The first gene of the *Bacillus subtilis clpC* operon, *ctsR*, encodes a
862 negative regulator of its own operon and other Class III heat shock genes. *J. Bacteriol.* **180**,
863 6681–6688 (1998).
864 4. Elsholz, A. K. W., Michalik, S., Zühlke, D., Hecker, M. & Gerth, U. CtsR, the Gram-positive master
865 regulator of protein quality control, feels the heat. *EMBO J.* **29**, 3621–3629 (2010).
866 5. Krüger, E., Witt, E., Ohlmeier, S., Hanschke, R. & Hecker, M. The Clp proteases of *Bacillus*
867 *subtilis* are directly involved in degradation of misfolded proteins. *J. Bacteriol.* **182**, 3259–3265
868 (2000).
869 6. Alver, R. *et al.* The control of protein arginine phosphorylation facilitates proteostasis by an AAA+
870 chaperone protease system. 2022.09.15.508104 Preprint at
871 https://doi.org/10.1101/2022.09.15.508104 (2023).
872 7. Schäfer, H. *et al.* The alarmones (p)ppGpp are part of the heat shock response of *Bacillus subtilis*.
873 *PLOS Genet.* **16**, e1008275 (2020).
874 8. Clay, K. J., Yang, Y., Clark, C. & Petrascheck, M. Proteostasis is differentially modulated by
875 inhibition of translation initiation or elongation. *eLife* **12**, e76465 (2023).
876 9. Cherkasov, V. *et al.* Coordination of translational control and protein homeostasis during severe
877 heat stress. *Curr. Biol.* **23**, 2452–2462 (2013).
878 10. Schramm, F. D., Schroeder, K. & Jonas, K. Protein aggregation in bacteria. *FEMS Microbiol. Rev.*
879 **44**, 54–72 (2020).
880 11. Schäfer, H. *et al.* Spx, the central regulator of the heat and oxidative stress response in *B. subtilis*
881 , can repress transcription of translation-related genes. *Mol. Microbiol.* mmi.14171 (2018)
882 doi:10.1111/mmi.14171.
883 12. Nakano, S., Erwin, K. N., Ralle, M. & Zuber, P. Redox-sensitive transcriptional control by a
884 thiol/disulphide switch in the global regulator, Spx. *Mol. Microbiol.* **55**, 498–510 (2005).
885 13. Runde, S. *et al.* The role of thiol oxidative stress response in heat-induced protein aggregate
886 formation during thermotolerance in *Bacillus subtilis*. *Mol. Microbiol.* **91**, 1036–1052 (2014).
887 14. Rochat, T. *et al.* Genome-wide identification of genes directly regulated by the pleiotropic
888 transcription factor Spx in *Bacillus subtilis*. *Nucleic Acids Res.* **40**, 9571–9583 (2012).
889 15. Diez, S., Ryu, J., Caban, K., Gonzalez, R. L. & Dworkin, J. The alarmones (p)ppGpp directly
890 regulate translation initiation during entry into quiescence. *Proc. Natl. Acad. Sci.* **117**, 15565–
891 15572 (2020).
892 16. Corrigan, R. M., Bellows, L. E., Wood, A. & Gründling, A. ppGpp negatively impacts ribosome
893 assembly affecting growth and antimicrobial tolerance in Gram-positive bacteria. *Proc. Natl. Acad.*
894 *Sci.* **113**, (2016).
895 17. Pausch, P. *et al.* Structural basis for (p)ppGpp-mediated inhibition of the GTPase RbgA. *J. Biol.*
896 *Chem.* **293**, 19699–19709 (2018).
897 18. Krásný, L., Tišerová, H., Jonák, J., Rejman, D. & Šanderová, H. The identity of the transcription
898 +1 position is crucial for changes in gene expression in response to amino acid starvation in
899 *Bacillus subtilis*. *Mol. Microbiol.* **69**, 42–54 (2008).
900 19. Krásný, L. & Gourse, R. L. An alternative strategy for bacterial ribosome synthesis: *Bacillus*
901 *subtilis* rRNA transcription regulation. *EMBO J.* **23**, 4473–4483 (2004).
902 20. Koo, B.-M. *et al.* Construction and analysis of two genome-scale deletion libraries for *Bacillus*
903 *subtilis*. *Cell Syst.* **4**, 291-305.e7 (2017).
904 21. Msadek, T. *et al.* ClpP of *Bacillus subtilis* is required for competence development, motility,
905 degradative enzyme synthesis, growth at high temperature and sporulation. *Mol. Microbiol.* **27**,
906 899–914 (1998).
907 22. Hajdusits, B. *et al.* McsB forms a gated kinase chamber to mark aberrant bacterial proteins for
908 degradation. *eLife* **10**, e63505 (2021).
909 23. Matavacas, J., Hallgren, J. & von Wachenfeldt, C. *Bacillus subtilis* forms twisted cells with cell wall
910 integrity defects upon removal of the molecular chaperones DnaK and trigger factor. *Front.*
911 *Microbiol.* **13**, (2023).
912 24. Schumann, W. Regulation of bacterial heat shock stimulons. *Cell Stress Chaperones* **21**, 959–968
913 (2016).

25. DeLoughery, A., Dengler, V., Chai, Y. & Losick, R. Biofilm formation by *Bacillus subtilis* requires an endoribonuclease-containing multisubunit complex that controls mRNA levels for the matrix gene repressor SinR. *Mol. Microbiol.* **99**, 425–437 (2016).
26. DeLoughery, A., Lalanne, J.-B., Losick, R. & Li, G.-W. Maturation of polycistronic mRNAs by the endoribonuclease RNase Y and its associated Y-complex in *Bacillus subtilis*. *Proc. Natl. Acad. Sci.* **115**, E5585–E5594 (2018).
27. Broglia, L. *et al.* An RNA-seq based comparative approach reveals the transcriptome-wide interplay between 3′-to-5′ exoRNases and RNase Y. *Nat. Commun.* **11**, 1587 (2020).
28. Taggart, J. C. *et al.* A high-resolution view of RNA endonuclease cleavage in *Bacillus subtilis*. *Nucleic Acids Res.* **53**, gkaf030 (2025).
29. Khemici, V., Prados, J., Linder, P. & Redder, P. Decay-initiating endoribonucleolytic cleavage by RNase Y is kept under tight control via sequence preference and sub-cellular localisation. *PLOS Genet.* **11**, e1005577 (2015).
30. Le Scornet, A. *et al.* Critical factors for precise and efficient RNA cleavage by RNase Y in *Staphylococcus aureus*. *PLOS Genet.* **20**, e1011349 (2024).
31. Shahbabian, K., Jamalli, A., Zig, L. & Putzer, H. RNase Y, a novel endoribonuclease, initiates riboswitch turnover in *Bacillus subtilis*. *EMBO J.* **28**, 3523–3533 (2009).
32. Chao, Y. *et al.* In vivo cleavage map illuminates the central role of RNase E in coding and non-coding RNA pathways. *Mol. Cell* **65**, 39–51 (2017).
33. Kime, L., Jourdan, S. S., Stead, J. A., Hidalgo-Sastre, A. & McDowall, K. J. Rapid cleavage of RNA by RNase E in the absence of 5′ monophosphate stimulation. *Mol. Microbiol.* **76**, 590–604 (2010).
34. Davis, J. H. & Williamson, J. R. Structure and dynamics of bacterial ribosome biogenesis. *Philos. Trans. R. Soc. B Biol. Sci.* **372**, 20160181 (2017).
35. Dubnau, E., DeSantis, M. & Dubnau, D. Formation of a stable RNase Y-RicT (YaaT) complex requires RicA (YmcA) and RicF (YlbF). *mBio* e01269-23 (2023) doi:10.1128/mbio.01269-23.
36. Eymann, C., Homuth, G., Scharf, C. & Hecker, M. *Bacillus subtilis* functional genomics: global characterization of the stringent response by proteome and transcriptome analysis. *J. Bacteriol.* **184**, 2500–2520 (2002).
37. Tagami, K. *et al.* Expression of a small (p)ppGpp synthetase, YwaC, in the (p)ppGpp^0 mutant of *Bacillus subtilis* triggers YvyD-dependent dimerization of ribosome. *MicrobiologyOpen* **1**, 115–134 (2012).
38. Beckert, B. *et al.* Structure of the *Bacillus subtilis* hibernating 100S ribosome reveals the basis for 70S dimerization. *EMBO J.* **36**, 2061–2072 (2017).
39. Carabetta, V. J. *et al.* A complex of YlbF, YmcA and YaaT regulates sporulation, competence and biofilm formation by accelerating the phosphorylation of Spo0A. *Mol. Microbiol.* **88**, 283–300 (2013).
40. Tortosa, P., Albano, M. & Dubnau, D. Characterization of *ylbF*, a new gene involved in competence development and sporulation in *Bacillus subtilis*. *Mol. Microbiol.* **35**, 1110–1119 (2000).
41. Branda, S. S. *et al.* Genes involved in formation of structured multicellular communities by *Bacillus subtilis*. *J. Bacteriol.* **186**, 3970–3979 (2004).
42. Segev, E., Smith, Y. & Ben-Yehuda, S. RNA dynamics in aging bacterial spores. *Cell* **148**, 139–149 (2012).
43. Hinrichs, R., Pozhydaieva, N., Höfer, K. & Graumann, P. L. Y-complex proteins show RNA-dependent binding events at the cell membrane and distinct single-molecule dynamics. *Cells* **11**, 933 (2022).
44. Adusei-Danso, F. *et al.* Structure-function studies of the *Bacillus subtilis* Ric proteins identify the Fe-S cluster-ligating residues and their roles in development and RNA processing. *mBio* **10**, e01841-19, /mbio/10/5/mBio.01841-19.atom (2019).
45. Lehnik-Habrink, M. *et al.* The RNA degradosome in *Bacillus subtilis*: identification of CshA as the major RNA helicase in the multiprotein complex. *Mol. Microbiol.* **77**, 958–971 (2010).
46. Commichau, F. M. *et al.* Novel activities of glycolytic enzymes in *Bacillus subtilis*. *Mol. Cell. Proteomics* **8**, 1350–1360 (2009).
47. Durand, S. & Condon, C. RNases and helicases in Gram-positive bacteria. *Microbiol. Spectr.* **6**, 10.1128/microbiolspec.rwr-0003–2017.
48. Dimitrova-Paternoga, L. *et al.* Structural basis of ribosomal 30S subunit degradation by RNase R. *Nature* **626**, 1133–1140 (2024).
49. Boylan, S. A., Redfield, A. R., Brody, M. S. & Price, C. W. Stress-induced activation of the Sigma B transcription factor of *Bacillus subtilis*. *J. Bacteriol.* **175**, 7931–7937 (1993).

50. Kirstein, J., Molière, N., Dougan, D. A. & Turgay, K. Adapting the machine: adaptor proteins for Hsp100/Clp and AAA+ proteases. *Nat. Rev. Microbiol.* **7**, 589–599 (2009).
51. Lehnik-Habrink, M. *et al.* RNA processing in *Bacillus subtilis*: identification of targets of the essential RNase Y: Targets of the essential RNase Y in *Bacillus subtilis*. *Mol. Microbiol.* **81**, 1459–1473 (2011).
52. Anderson, B. W., Fung, D. K. & Wang, J. D. Regulatory themes and variations by the stress-signaling nucleotide alarmones (p)ppGpp in bacteria. *Annu. Rev. Genet.* **55**, 115–133 (2021).
53. Driller, K., Cornejo, F. A. & Turgay, K. (p)ppGpp – an important player during heat shock response. *microLife* **4**, uqad017 (2023).
54. Zundel, M. A., Basturea, G. N. & Deutscher, M. P. Initiation of ribosome degradation during starvation in *Escherichia coli*. *RNA* **15**, 977–983 (2009).
55. Sulthana, S., Basturea, G. N. & Deutscher, M. P. Elucidation of pathways of ribosomal RNA degradation: an essential role for RNase E. *RNA* **22**, 1163–1171 (2016).
56. Lehnik-Habrink, M. *et al.* RNase Y in *Bacillus subtilis*: a natively disordered protein that is the functional equivalent of RNase E from *Escherichia coli*. *J. Bacteriol.* **193**, 5431–5441 (2011).
57. Marcaida, M. J., DePristo, M. A., Chandran, V., Carpousis, A. J. & Luisi, B. F. The RNA degradosome: life in the fast lane of adaptive molecular evolution. *Trends Biochem. Sci.* **31**, 359–365 (2006).
58. Piir, K., Paier, A., Liiv, A., Tenson, T. & Maiväli, Ü. Ribosome degradation in growing bacteria. *EMBO Rep.* **12**, 458–462 (2011).
59. Kuroda, A. *et al.* Role of inorganic polyphosphate in promoting ribosomal protein degradation by the Lon protease in *E. coli*. *Science* **293**, 705–708 (2001).
60. An, H. & Harper, J. W. Ribosome abundance control via the ubiquitin–proteasome system and autophagy. *J. Mol. Biol.* **432**, 170–184 (2020).
61. Huang, Z. *et al.* RIOK3 mediates the degradation of 40S ribosomes. *Mol. Cell* **85**, 802-814.e12 (2025).
62. Ford, P. W. *et al.* RNF10 and RIOK3 facilitate 40S ribosomal subunit degradation upon 60S biogenesis disruption or amino acid starvation. *Cell Rep.* **44**, 115371 (2025).
63. Coria, A. R. *et al.* The integrated stress response regulates 18S nonfunctional rRNA decay in mammals. *Mol. Cell* **85**, 787-801.e8 (2025).
64. Simpkins, S. W. *et al.* Using BEAN-counter to quantify genetic interactions from multiplexed barcode sequencing experiments. *Nat. Protoc.* **14**, 415–440 (2019).
65. Benjamini, Y. & Hochberg, Y. Controlling the false discovery rate: a practical and powerful approach to multiple testing. *J. R. Stat. Soc. Ser. B Methodol.* **57**, 289–300 (1995).
66. Lécrivain, A.-L. *et al.* In vivo 3′-to-5′ exoribonuclease targetomes of *Streptococcus pyogenes*. *Proc. Natl. Acad. Sci.* **115**, 11814–11819 (2018).
67. Martin, M. Cutadapt removes adapter sequences from high-throughput sequencing reads. *EMBnet.journal* **17**, 10 (2011).
68. Dobin, A. *et al.* STAR: ultrafast universal RNA-seq aligner. *Bioinformatics* **29**, 15–21 (2013).
69. Li, H. *et al.* The Sequence Alignment/Map format and SAMtools. *Bioinformatics* **25**, 2078–2079 (2009).
70. Smith, T., Heger, A. & Sudbery, I. UMI-tools: modeling sequencing errors in Unique Molecular Identifiers to improve quantification accuracy. *Genome Res.* **27**, 491–499 (2017).
71. Liao, Y., Smyth, G. K. & Shi, W. featureCounts: an efficient general purpose program for assigning sequence reads to genomic features. *Bioinformatics* **30**, 923–930 (2014).
72. Love, M. I., Huber, W. & Anders, S. Moderated estimation of fold change and dispersion for RNA-seq data with DESeq2. *Genome Biol.* **15**, 550 (2014).
73. Putri, G. H., Anders, S., Pyl, P. T., Pimanda, J. E. & Zanini, F. Analysing high-throughput sequencing data in Python with HTSeq 2.0. *Bioinformatics* **38**, 2943–2945 (2022).
74. Mölder, F. *et al.* Sustainable data analysis with Snakemake. Preprint at https://doi.org/10.12688/f1000research.29032.2 (2021).
75. McCarthy, D. J., Chen, Y. & Smyth, G. K. Differential expression analysis of multifactor RNA-Seq experiments with respect to biological variation. *Nucleic Acids Res.* **40**, 4288–4297 (2012).
76. Geissler, A. S. *et al.* BSGatlas: a unified *Bacillus subtilis* genome and transcriptome annotation atlas with enhanced information access. *Microb. Genomics* **7**, 000524 (2021).
77. Tareen, A. & Kinney, J. B. Logomaker: beautiful sequence logos in Python. *Bioinformatics* **36**, 2272–2274 (2020).
78. Lorenz, R. *et al.* ViennaRNA Package 2.0. *Algorithms Mol. Biol.* **6**, 26 (2011).
79. Elfmann, C., Dumann, V., van den Berg, T. & Stülke, J. A new framework for SubtiWiki, the database for the model organism *Bacillus subtilis*. *Nucleic Acids Res.* **53**, D864–D870 (2025).

80. Pfaffl, M. W. A new mathematical model for relative quantification in real-time RT-PCR. *Nucleic Acids Res.* **29**, 45e–445 (2001).
81. Hughes, C. S. *et al.* Single-pot, solid-phase-enhanced sample preparation for proteomics experiments. *Nat. Protoc.* **14**, 68–85 (2019).
82. Kohler, D. *et al.* MSstats version 4.0: statistical analyses of quantitative mass spectrometry-based proteomic experiments with chromatography-based quantification at scale. *J. Proteome Res.* **22**, 1466–1482 (2023).
83. Jahn, M. *et al.* Growth of cyanobacteria is constrained by the abundance of light and carbon assimilation proteins. *Cell Rep.* **25**, 478-486.e8 (2018).
84. Jahn, M. *et al.* Protein allocation and utilization in the versatile chemolithoautotroph *Cupriavidus necator*. *eLife* **10**, e69019 (2021).
85. Sohmen, D. *et al.* Structure of the *Bacillus subtilis* 70S ribosome reveals the basis for species-specific stalling. *Nat. Commun.* **6**, 6941 (2015).

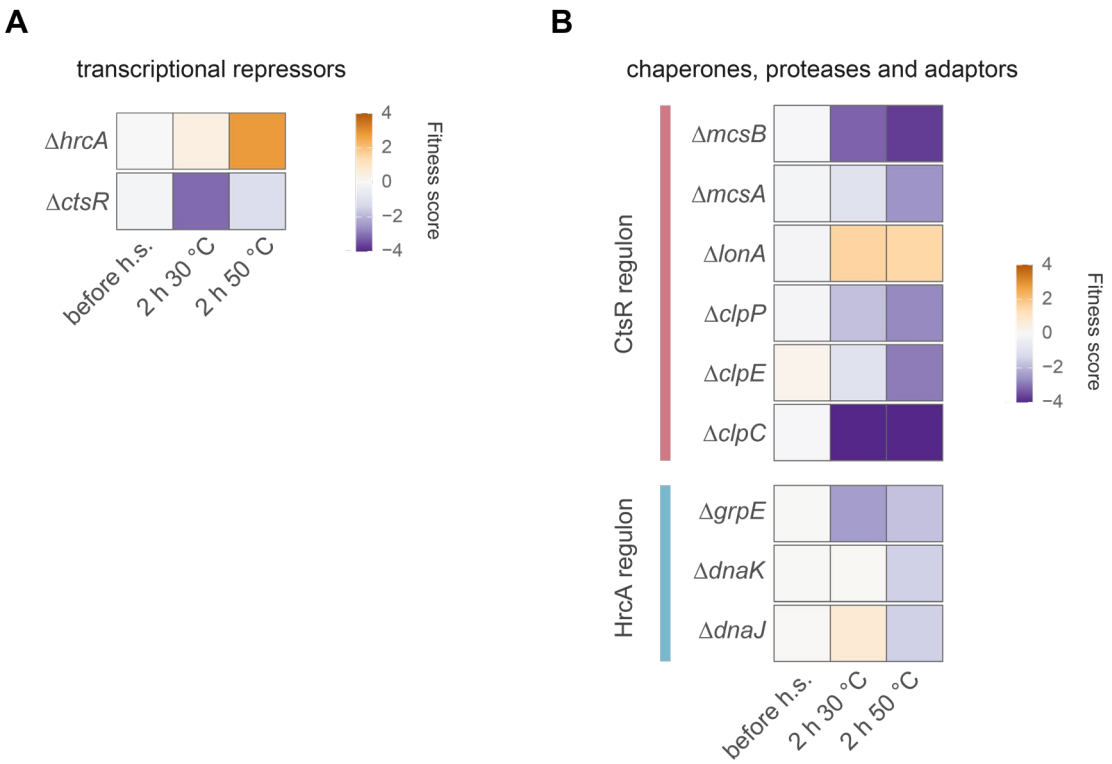

1048

1049 **Supplementary Figure 1. Fitness of selected deletion mutants during heat shock in the genetic**
1050 **screening.** Heatmap of the relative fitness of **A)** heat shock transcriptional repressors, and **B)**
1051 chaperones, proteases and adaptors. The color represents the average relative fitness of three
1052 biological replicates. A negative relative fitness value means that the abundance of the deletion mutant,
1053 compared to the rest of the population, was negatively affected by the treatment, while a positive value
1054 means an increased abundance on those conditions. h.s. = heat shock.

1055

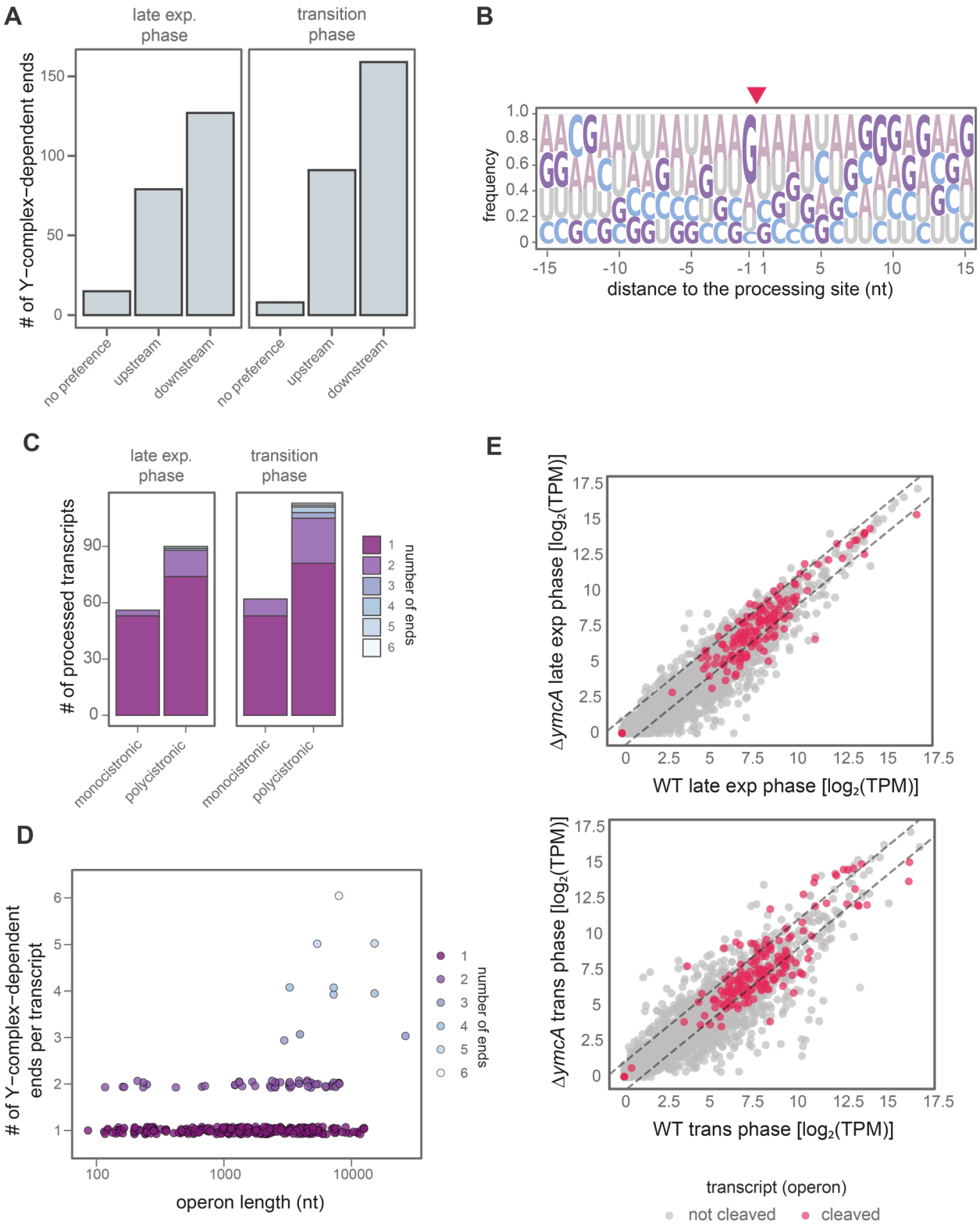

Supplementary Figure 2. Recognition motif, length, or expression levels do not determine the Y-complex substrates. A) Stabilization of the resulting fragments after Y-complex processing, the coverage ratio in a window of 5 nt before and after the processing site was calculated and used as a proxy of the stabilization of the resulting fragments. The predicted stability correlates with the end detected in the ISCP method. **B)** Motif search using 5' and U-type ends. The arrow indicates the cleavage site. **C)** Number of Y-complex-dependent cleavages detected per monocistronic or polycistronic transcripts in the late exponential or transition phase. **D)** Number of cleavages detected by

1064 operon length of the transcript. The color indicates the numbers of Y-complex-dependent ends detected
1065 per transcript **E)** RNA levels of WT and Δ*ymcA* mutant transcripts at late exponential and transition
1066 phases. Transcripts processed by the Y-complex are highlighted in magenta. Transcript annotations
1067 were obtained from BSGatlas.

1068

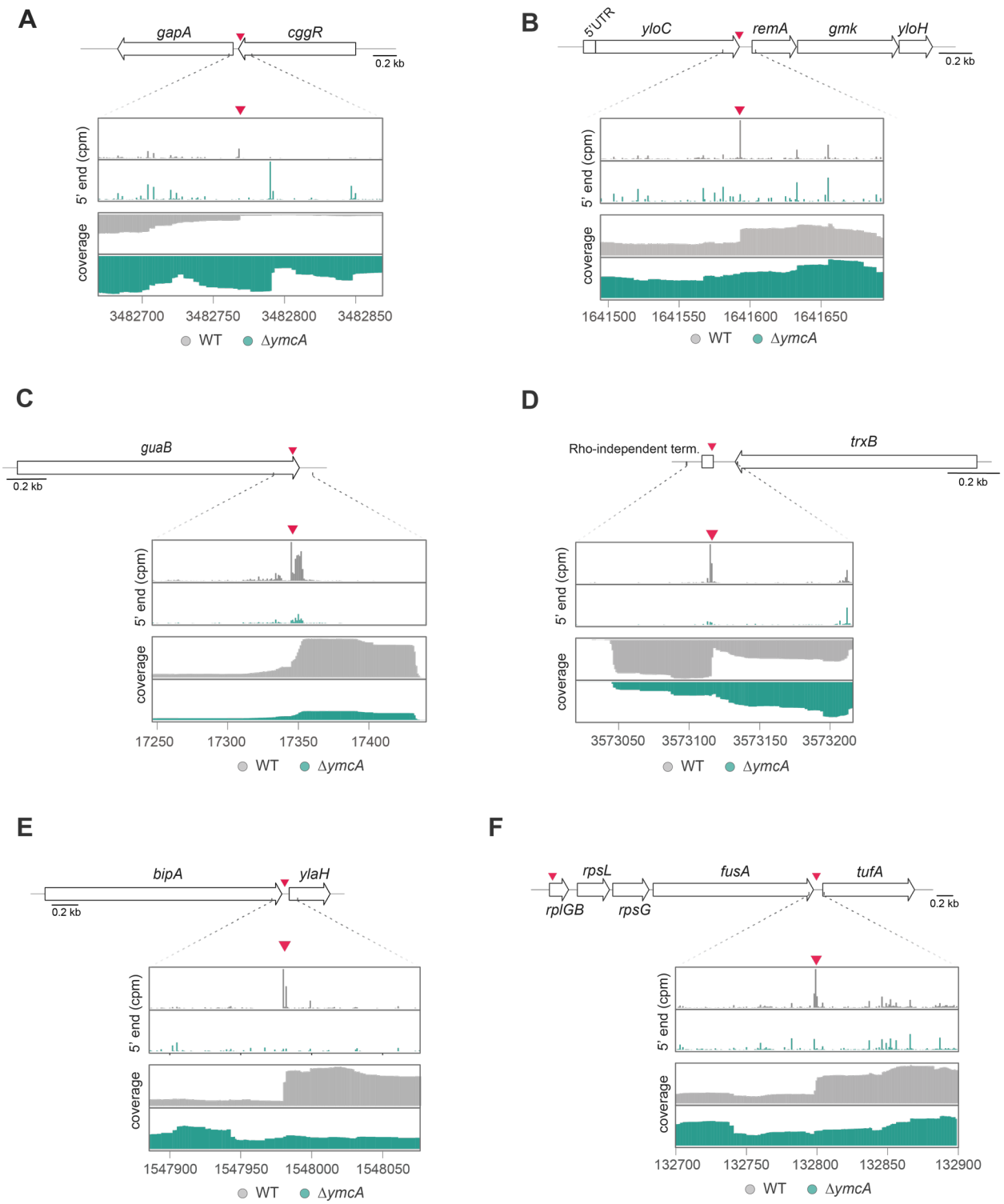

Supplementary Figure 3. The Y-complex processes mRNA in UTRs and coding regions. RNA end counts per million (cpm), and RNA-seq coverage of selected transcripts in WT and Δ*ymcA.* The arrow indicates the Y-complex-dependent processing site. **A)** The *gapA-cggR* transcript was used as a positive control. **B)** Processing in the coding region of *yloC* in the polycistronic mRNA *yloC-remA-gmk-yloH*. **C)** Processing in the coding region of the monocistronic transcript of *guaB*. **D)** Processing at the 3' UTR of *trxB,* near the Rho-independent terminator. Processing in the internal UTR of translation-associated transcripts like **E)** the *bipA-ylaH* transcript, and **F)** between *fusA-tufA*.

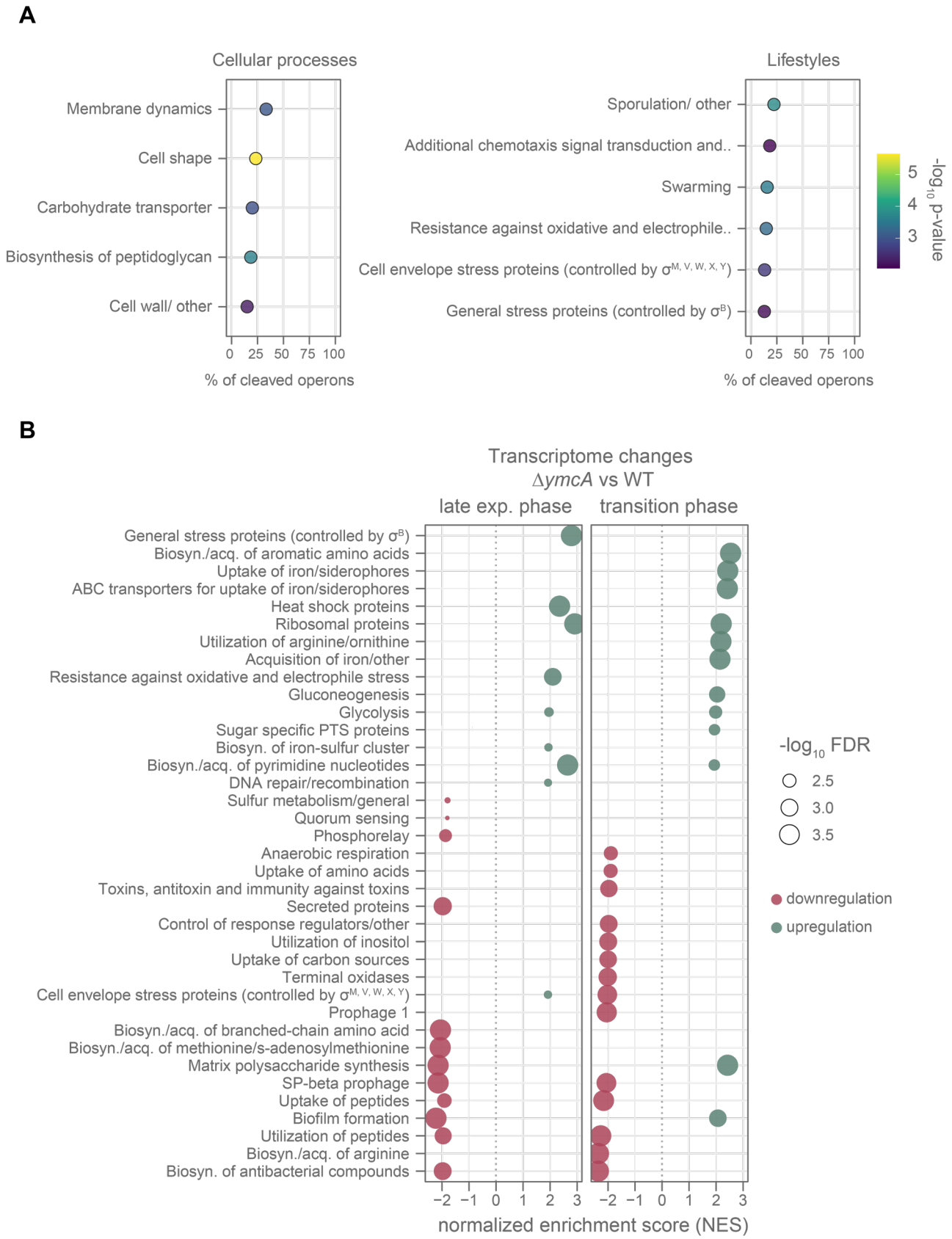

Supplementary Figure 4. mRNA processing by the Y-complex and effect on the transcriptome. A) Overrepresentation analysis of pathways whose transcripts are cleaved by the Y-complex during the late exponential phase. Operons were assigned to be involved in a pathway if they code for one gene

1081 participating in such a pathway. Pathway annotations were retrieved from SubtiWiki[79]. The color
1082 indicates the statistical significance of the enrichment. **B)** Gene set enrichment analysis (GSEA) of
1083 differentially expressed genes at the late exponential and transition phase when comparing Δ*ymcA* to
1084 WT. The size of the dot represents the statistical significance. The normalized enrichment score is
1085 displayed on the *x*-axis; positive values mean upregulation; meanwhile negative values mean
1086 downregulation. GSEA results were prefiltered for pathways showing and enrichment with an FDR ≤
1087 0.01. Biosyn. = Biosynthesis, acq. = Acquisition.

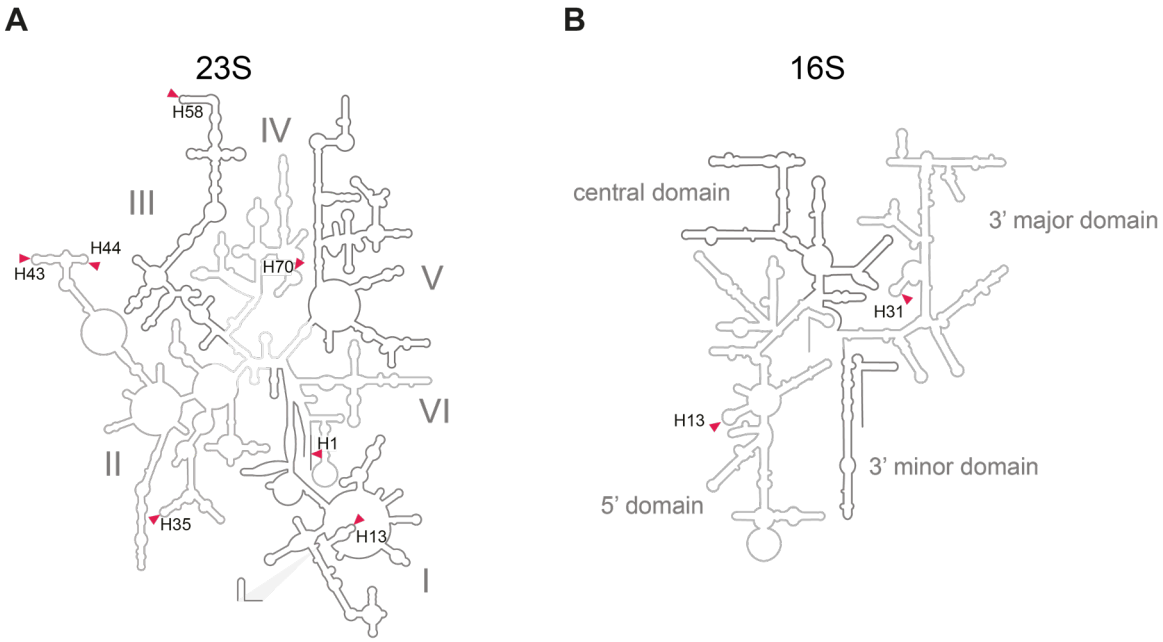

1088

1089 **Supplementary Figure 5. Mapping of Y-complex-dependent processing in the secondary**
1090 **structure of rRNA at the late exponential phase.** Cleavages are marked with an arrow and the helix
1091 number for **A)** 23S and **B)** 16S rRNA.

1092

Supplementary Figure 6. Mapping of Y-complex dependent processing in the ribosome 3D structure. The RNA end detected by the ISCP method is highlighted in magenta. The ribosome structure was retrieved from PDB (ID: 3J9W)[85]. The A site is shown as a green ellipse.

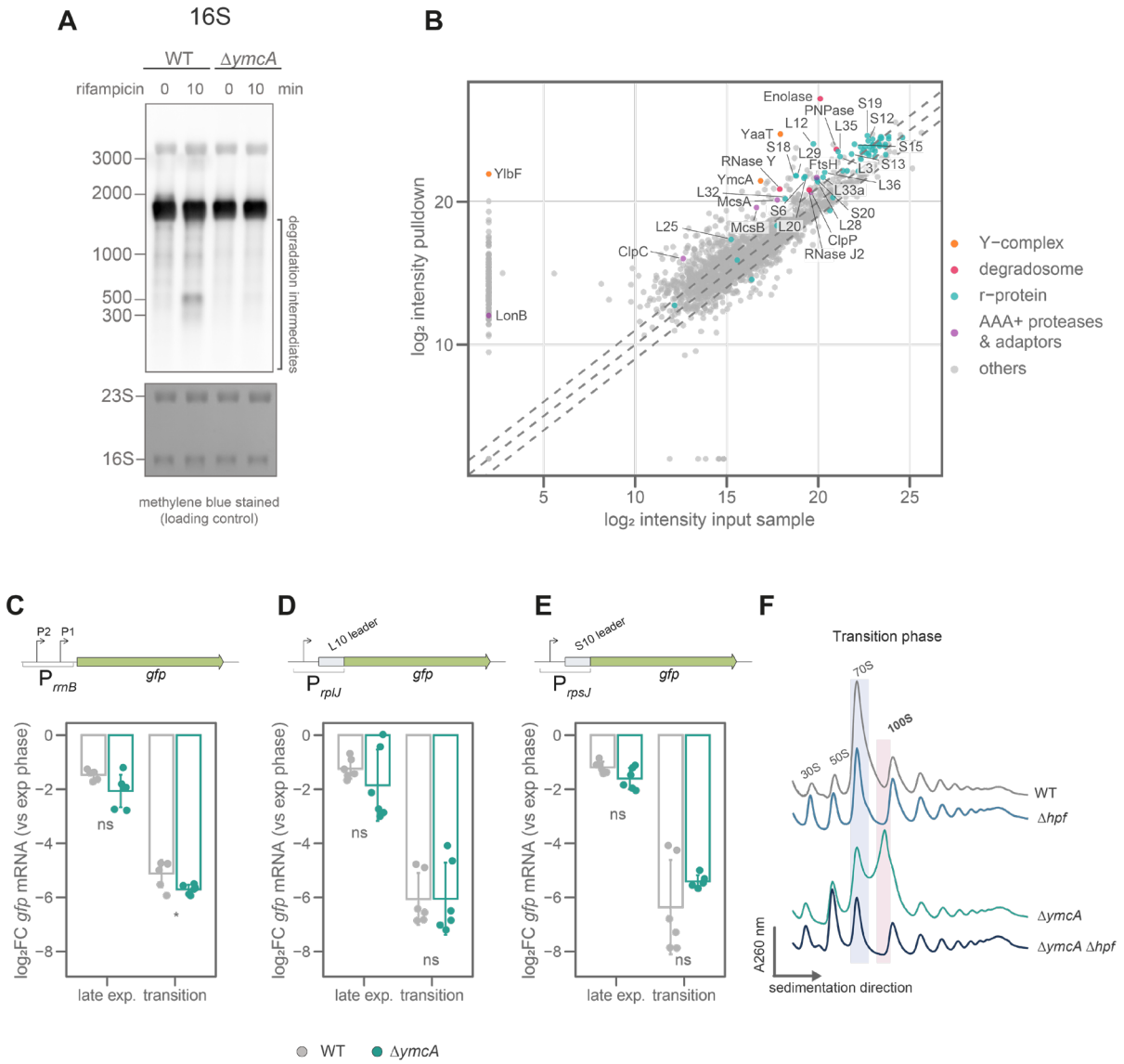

Supplementary Figure 7. Y-complex-dependent initiates degradation of rRNA but does not affect transcriptional control of stringent response. A) Northern blot against 16S of WT and Δ*ymcA* cells at the late exponential phase, before and after treatment with 100 µg/ml rifampicin to inhibit transcription. The methylene blue-stained membrane is shown as a loading control. This image is representative of three biological replicates. **B)** Pulldown of YaaT-FLAG at the late exponential phase. The protein intensities of the input sample and the elution fraction were measured by mass spectrometry. The dotted lines indicate a fold change of less than 2. A $\log_2$ intensity value of two was inputed when a protein was missing in one of the samples. Activity of the promoter controlling **C)** *rrnB* (rRNA) transcription, **D)** *rplJ*, and **E)** *rpsJ* (r-proteins) genes at late exponential and transition phase compared to the exponential phase in WT and Δ*ymcA*. The promoters were cloned controlling *gfp* transcription, which was measured using RT-qPCR. The *pcp* transcript was used as a reference. Individual values and the average ± standard deviation of three biological replicates and two technical replicates are shown. The statistical significance was tested using student's *t*-test. ns: *p*-value > 0.05, *: *p*-value ≤ 0.05. **F)** Ribosome sedimentation profile in 10-50% sucrose gradients of WT, Δ*hpf,* Δ*ymcA,* and Δ*ymcA* Δ*hpf* in the transition phase. The 70S and 100S ribosomes are highlighted with a blue or red box, respectively. The data is representative of three biological replicates.

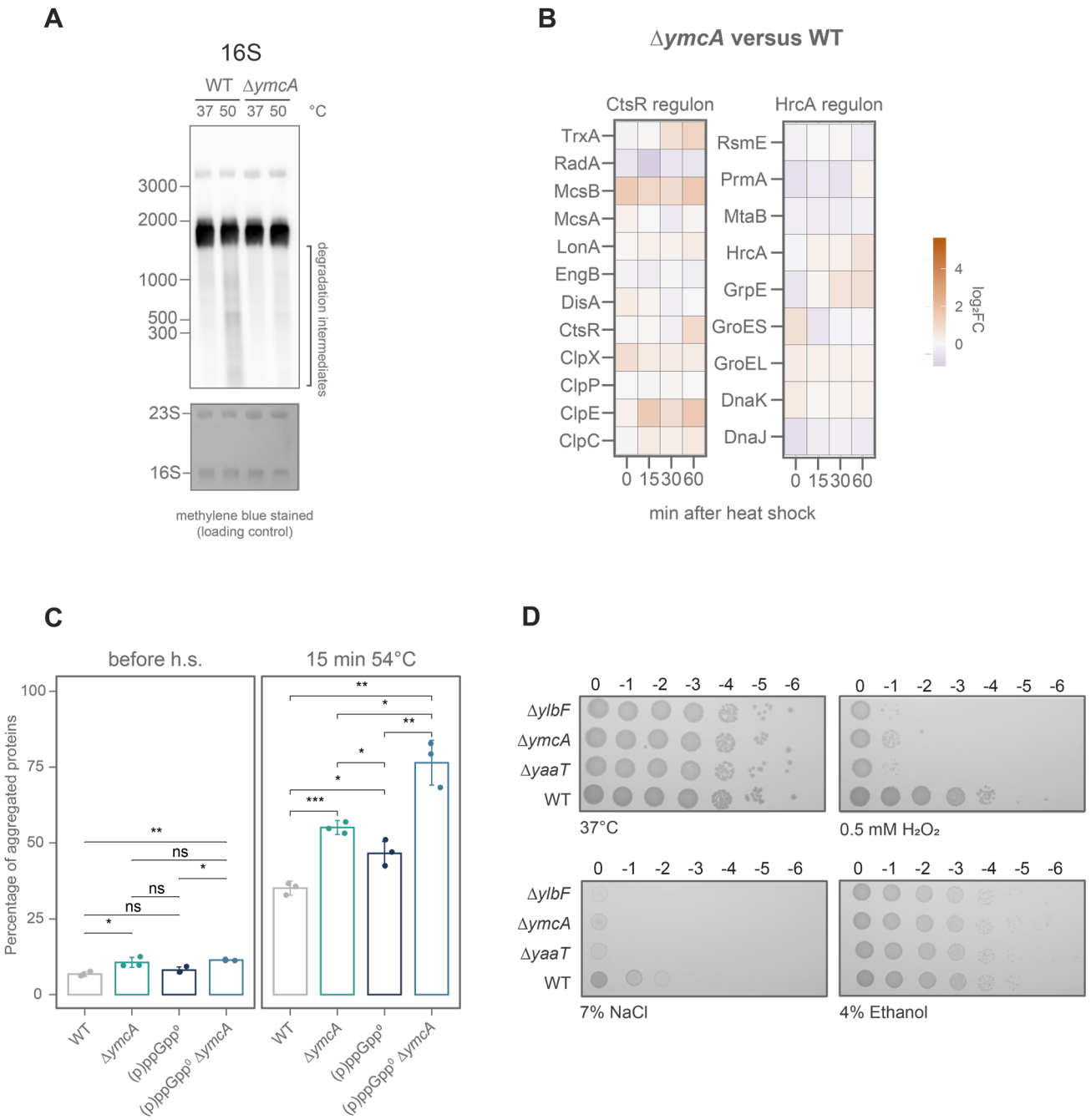

Supplementary Figure 8. Control of ribosome levels and protein homeostasis in *ymcA* is important for responding against proteotoxic stresses. A) Northern blot against 16S of WT and Δ*ymcA* cells at exponential phase before and after heat shock. The methylene blue-stained membrane is shown as a loading control. This image is representative of three biological replicates. **B)** Induction of CtsR and HrcA regulons after heat shock (50°C) Δ*ymcA* compared to the WT. Proteins were measured by mass spectrometry. The color bar shows the $\log_2$ fold change compared to the WT control. **C)** Percentage of aggregated proteins before and after a 15 min heat shock at 54°C in WT and Δ*ymcA*, (p)ppGpp^0 and (p)ppGpp^0 Δ*ymcA*. Individual values and the average ± standard deviation of three biological replicates are shown. The statistical difference was tested using student's *t*-test. ns: *p*-value > 0.05, *: *p*-value ≤ 0.05, **: *p*-value ≤ 0.01, ***: *p*-value ≤ 0.001. **D)** Spot test of deletion mutants of Y-complex members in the displayed stresses. The picture is representative of three biological replicates.